Reply to Anonymous Referee #1 (amt-2019-311-AC1):

Atmospheric aerosols play a crucial role in regional radiative budgets. The changes in surface radiation induced by aerosols significantly impacts the surface temperature, crop growth and solar energy availability. However, the current assessment of aerosol direct radiative forcing (ADRF) remains highly uncertain. This paper proposes the method for ADRF simulation in East China based on a combination of MODIS and MERRA model reanalysis data. The comparison with surface measurements ensures the accuracy of this retrieval, and it is the highlight of this research along with detailed discussion about error analysis. The analysis of ADRF distribution provides valuable information about the aerosol radiative effect in the heavily polluted region, East China, and in the period when it experienced an unprecedented economic boom. This method is helpful to study aerosol-induced changes in the surface radiation un-der climate change and agricultural economic impact over China. The research makes an interesting and potentially useful contribution. However, there are several points need to be addressed and revise carefully. Overall, I recommend this manuscript for publication in AMT with Minor Revision.

Response:

We appreciate the positive comments of the Referee. It is your valuable comments that make this manuscript more scientific and rational. We have studied the comments carefully and tried our best to revise our manuscript accordingly. Some errors and deficiencies were also revised through our self-check process. We would like to express our thanks for the constructive comments again, and we look forward to hearing your feedback. The specific corrections and comments that are addressed below.

General comments:

1. **The most important factor affecting ADRF simulation is the accuracy of MERRA -2 SSA in East China. I notice that the chosen sunphotometers all locate in the northern China, these sites may not represent the whole East China, what comparison results in other sunphotometers of East China?**

R: Thanks for the insight comments and I totally agree with the reviewer's opinion. Here, we found all

the SSA data from the open source (AERONET, http://aeronet.gsfc.nasa.gov/). All sunphotometer sites over East China were collected to validate with MERRA-2 SSA. Six sites of East China were chosen, that is, Xuzhou, Shouxian, Hefei, Taihu, Pudong and Hangzhou. The detail information of site locations and the comparisons between MERRA-2 and sunphotometer SSA are shown in Table 3 and Figure 3. The validation results also have been analyzed:

"The location of the sunphotometers was shown in Figure 3(a), and their geographical characteristics, observation periods, sample numbers as well as the fitted regression equation between MERRA-2 and sunphotometer SSA were presented in Table 3. In East China, six sunphotometer sites, Xuzhou (117.14ºE, 34.22ºN), Shouxian (116.78ºE, 32.56ºN), Hefei (117.16ºE, 31.91ºN), Taihu (120.22ºE, 31.42ºN), Pudong (121.79ºE, 31.05ºN) and Hangzhou (120.16ºE, 30.29ºN) (Figure 3a), were chosen for comparison with MERRA-2 SSA data. Table 3 shows the locations of these sunphotometers, and their geographical characteristics, observing periods as well as fitted regression equation between MERRA-2 and sunphotometer SSA. The detailed comparisons at Xuzhou, Shouxian and Hefei were shown in the Figure 3b. Orange dots represent Xuzhou samples and orange line is the according fitting curve, while green represents Shouxian, and black is Hefei. Figure 3c displays the comparison results at Taihu, Pudong and Hangzhou. Red denotes Taihu, purple is Pudong and yellow is Hangzhou. As shown in Figure 3, dashed lines are the range of ±10% relative error, all samples in Taihu, Pudong and Hefei, 94% of samples in Xuzhou, 93% in Shouxian and 98% in Hangzhou fall within the ±10% error. This finding suggests that MERRA-2 SSA agrees well with the sunphotometer data, even though few SSA samples are beyond the error range. Furthermore, the slopes of linear fitting curve are less than 1 at all sites except Shouxian (Table 3), and it reveals that MERRA-2 SSA has systematic biases at most area of East China."

Table 3: The geographical characteristics, observing period, sample number of sunphotometer sites. The fitted regression equations between MERRA-2 and sunphotometer SSA are also shown here. In the equation, x represents SSA sample, y represents fitted value of SSA.

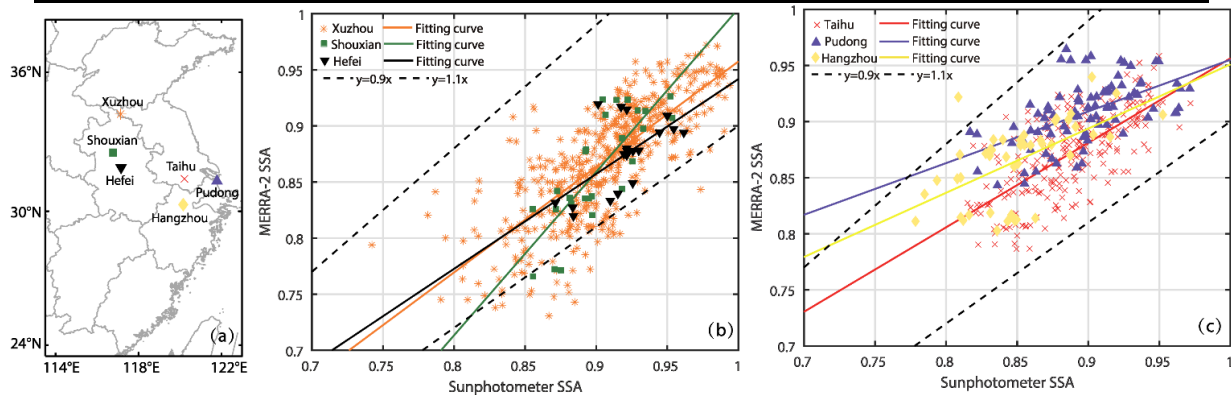| Location	Lon/Lat	Observing period	Sample number	Fitted regression equation between MERRA-2 and sunphotometer SSA
Xuzhou (Urban)	117.14°E/34.22°N	2013.8-2016.12	514	y=0.02+0.94x
Shouxian (Rural)	116.78°E/32.56°N	2008.5-2008.12	26	y=-0.45+1.46x
Hefei (Urban)	117.16°E/31.91°N	2005.11-2005.12 2008.1-2008.11	19	y=0.09+0.85x
Taihu (Rural)	120.22°E/31.42°N	2005.1-2012.12 2015.1-2016.12	230	y=0.2+0.75x
Pudong (Urban)	121.79°E/31.05°N	2010.12-2012.10 2014.1-2015.11	84	y=0.49+0.46x
Hangzhou (Urban)	120.16°E/30.29°N	2008.4-2009.2	45	y=0.38+0.57x

Figure 3: (a) The location of six sunphotometer sites over East China. (b) The scatter plots of SSA between MERRA-2 and sunphotometer in Xuzhou, Shouxian and Hefei. Orange dots represent Xuzhou samples and orange line is the fitting curve of Xuzhou samples while green represents Shouxian and black represents Hefei. Dashed lines are the range of ±10% relative error. (c) The scatter plots of SSA between MERRA-2 and sunphotometer in Taihu, Pudong and Hangzhou. Red dots represent Taihu samples and red line is the fitting curve of Taihu samples while purple denotes Pudong and yellow is Hangzhou. Dashed lines are the range of ±10% relative error.

2. **It seems chaotic in the error analysis of ADRF. In section 4.2, the author analyses the error sources between simulated F_d_sur and the observations (cloud contamination, different spatial and temporal representativeness. Is this associated with ADRF errors? In section 4.4, the author also conducts the uncertainty analysis of different aerosol optical parameters. The difference between this should be clarified, more explanations and structure adjustment are also needed.**

R: We thanks for your insight comments. The object of Section 4.2 is F_d_sur and Section 4.3 is ADRF. Section 4.2 discusses the specific validation cases, and the error sources have indeed impact on ADRF. However, the goal of uncertainty analysis in Section 4.4 is to quantify how much uncertainty of ADRF induced by the inputs (AOD, SSA, albedo, etc.). In general, the object of two sections are different, and for clarification, the uncertainty analysis in Section 4.4 has been moved to Section 4.3 in the revised manuscript.

3. **In Line 313, "the magnitude of ADRF is higher than most cities in the world, such as Spain (Esteve et al., 2014), Gasan (Kim et al., 2006) and Karachi (Alam et al., 12011)". It is suggested to add some more discussions about the comparison between East China and other countries. For example, why is ADRF in East China higher than other countries?**

R: Thanks for your suggestion. The more discussions about the comparison between East China and other countries have been added in the revised manuscript:

"The main reason is that AOD in East China is much larger than these cities, since East China has experienced rapid urbanization and economic development in the past 17 years and AOD is much larger than these regions. For example, mean AOD in East China is 0.62 in this study during 2003-2011 while AOD is 0.19 in Spain during 2003-2011 (Esteve et al., 2014)."

Reference:

Esteve A R, Estellés, V, Utrillas, María P, and Martínez-Lozano J.A.: Analysis of the aerosol radiative forcing over a Mediterranean urban coastal site. Atmos. Res., 137,195-204. http://dx.doi.org/10.1016/j.atmosres.2013.10.009, 2014.

Specific comments:

1. **Line 68: "Furthermore, aerosol microphysical parameters are crucial in ADRF simulation, including single scattering albedo and the asymmetry parameter (ASY), but their retrieval remains challenging." It is suggested to adjust word order for readability, for example, it is better to be written: "Furthermore, the retrieval of aerosol microphysical parameters remains challenging, including single scattering albedo and the asymmetry parameter (ASY)."**

R: Thanks for your suggestion. The sentence in Line 68 has been rephrased:

"Furthermore, the retrieval of aerosol microphysical parameters remains challenging, including single scattering albedo and the asymmetry parameter (ASY)."

2. **Line 161: "Before ADRF simulation, one of the inputs, SSA from MERRA-2, was evaluated firstly". Why does the author evaluate SSA first in the Results? Please make some more explanation about the goal of the SSA evaluation at the beginning of the Results.**

R: We appreciate your opinion. Before ADRF simulations, all the inputs are need to ensure their accuracy. Previous studies have never performed the validation of MERRA-2 SSA product. The according explanation about the goal of SSA evaluation has been added in the revised manuscript:

"Before ADRF simulation, one of the inputs, SSA from the accuracy of MERRA-2 SSA product, was evaluated firstly."

3. **Line 276: "MERRA-2 SSA is always underestimated in these conditions, potentially leading to the negative errors in the simulated F_d_sur". Why?**

R: The discussion about "the effect of aerosol sources" has some mistakes. Aerosols from north and south are different degree of scattering, but it cannot explain the different error sign. So, these associated sentences have been deleted in the manuscript.

4. **There are some mistakes in grammar in this paper, please check them carefully. For example, Line 19: "has" should be "have"; Line 57 "restricted" should be "are restricted"; Line 92: "including" should be "includes".**

R: Thanks for your careful suggestions. The according mistakes have been corrected, and some other grammar errors were also revised in the manuscript through our self-check process.

Retrieval of Gridded Aerosol Direct Radiative Forcing Based on Multiplatform Datasets

Yanyu Wang[1], Rui Lyu[1], Xin Xie[1], Ze Meng[8,2], Meijin Huang[3,2], Junshi Wu[4,3], Haizhen Mu[4,3], Qiu-Run Yu[4,5], Qianshan He[4,3,6,5]*, Tiantao Cheng[6,7,7,8,1]*

[1]Shanghai Key Laboratory of Atmospheric Particle Pollution and Prevention (LAP[3]), Department of Environmental Science and Engineering, Institute of Atmospheric Sciences, Fudan University, Shanghai, 200438, China
[2]School of Oceanography, Shanghai Jiao Tong University, Shanghai, 200030, China
[2,3]Fujian Meteorological Observatory, Fuzhou, 350001, China
[3,4]Shanghai Meteorological Service, Shanghai, 200030, China
[4,5]Key Laboratory of Meteorological Disaster, Ministry of Education (KLME)/Joint International Research Laboratory of Climate and Environment Change (ILCEC), Nanjing University of Information Science and Technology, Nanjing, 210044, China
[5,6]Shanghai Key Laboratory of Meteorology and Health, Shanghai, 200030, China.
[6,7]Department of Atmospheric and Oceanic Sciences, Institute of Atmospheric Sciences, Fudan University, Shanghai, 200438, China
[8,7]Shanghai Institute of Eco-Chongming (SIEC), Shanghai, 200062, China

Correspondence to: Qianshan He (oxeye75@163.com); Tiantao Cheng(ttcheng@fudan.edu.cn).

Abstract. Atmospheric aerosols play a crucial role in regional radiative budgets. Previous studies on clear-sky aerosol direct radiative forcing (ADRF) have mainly been limited to site-scale observations or model simulations for short-term cases, and long-term distributions of ADRF in China has not been portrayed yet. In this study, an accurate fine-resolution ADRF estimate at the surface was proposed. Multiplatform datasets, including satellite (MODIS aboard Terra and Aqua MODIS) and reanalysis datasets, served as inputs to the Santa Barbara Discrete Atmospheric Radiative Transfer (SBDART) model for ADRF simulation with consideration of the aerosol vertical profile over East China during 2000-2016. Specifically, single scattering albedo (SSA) from the Modern-Era Retrospective Analysis for Research and Application, version 2 (MERRA-2) was validated with sunphotometers over East China. The gridded asymmetry parameter (ASY) was then simulated by matching the calculated top-of-atmosphere (TOA) radiative fluxes from the radiative transfer model with satellite observations (Clouds and the Earth's Radiant Energy System (CERES)). The high correlation and small discrepancy (6-8 W m^{-2}) between simulated and observed radiative fluxes at three sites (Baoshan, Fuzhou, and Yong'an) indicated that ADRF retrieval is feasible and has high accuracy over East China. Then this method was applied in each grid of East China, and the overall picture of ADRF distributions over East China during 2000-2016 was displayed. ADRF ranges from -220 to -20 W m^{-2}, and annual mean ADRF is -100.21 W m^{-2}, implying that aerosols have strong cooling effect at the surface in East China during past 16 years. With the economic development and rapid urbanization, the spatiotemporal changes of ADRF during past 17 years are mainly attributed to the changes of anthropogenic emissions in East China. Finally, uncertainty analysis was also evaluated. Our method provides the long-term ADRF distribution over East China for the first time, with highlighting the importance of aerosol radiative impact under the climate change.

7

1 Introduction

Atmospheric aerosols play a significant role in air quality, regional/global climate and human health (Wang et al., 2018; Wang et al., 2019). Aerosols can directly absorb and scatter solar radiation, and indirectly affect cloud formation and precipitation by acting as cloud condensation nuclei or ice nuclei (Twomey, 1977; Rosenfeld, 1999). Large amounts of scattering aerosols can generally attenuate incoming solar radiation. This reduction in surface radiation significantly impacts the surface temperature, crop growth and solar energy availability (Chameides, 1999; Liao et al., 201~~6~~5). On the other hand, highly absorbing aerosols, such as black carbon, can warm the atmosphere, alter regional atmospheric stability, and even influence the large-scale circulation and hydrologic cycle with significant regional climate effects (Menon et al., 2002; Wang, J. et al., 2009). Aerosol direct radiative forcing (ADRF) is a good metric for evaluating the impact of aerosols to radiation by absorption and scattering, and is defined as the difference between the net radiative flux of earth-atmosphere systems with and without aerosols. Anthropogenic aerosols produce <u>a global mean negative direct radiative forcing of</u> -0.35±0.5 W m^{-2} of ADRF, which has dampened the warming effect of greenhouse gases (IPCC, 2013). However, the current assessment of ADRF remains highly uncertain. This uncertainty mainly results from the large variations in aerosol concentrations, chemical compositions, optical properties, mixing states, and vertical profiles (Haywood and Boucher, 2000; Tian et al., 2018a). Therefore, an accurate and feasible method for ADRF retrieval is greatly required.

Reduction in these uncertainties requires the integration of different techniques and datasets (e.g., surface measurement, model simulation, and satellite remote sensing) (Yu et al., 2006). To better understand aerosol optical properties and their radiative effect, several ground-based networks have been established worldwide, such as the AEROsol Robotic Network (AERONET) (Holben et al., 2001), Global Atmosphere Watch-Precision Filter Radiometer network (GAW-PFR) (Nyeki et al., 20~~0~~15), China Aerosol Remote Sensing Network (CARSNET) (Che et al., 2009) and Chinese Sun Hazemeter Network (CSHNET) (Xin et al., 2007). Moreover, intensive field experiments have been carried out over China, ~~and these measurements imply that aerosols exert different levels of cooling effect near the surface in different regions,~~ such as Beijing, Xianghe, Taihu, Wuhan, Shanghai, Lanzhou (Li et al., 2003; He et al., 2012a; Wang et al., 2014; Yu et al.,2016a; Gong et al., 2017; Zhang et al.,2018). Such measurements are conducive to <u>the</u> wider knowledge of aerosol properties, which are helpful for improving the performance of satellite and model simulations through synthesis. Nevertheless, ~~the~~ available measurements <u>are</u> usually restricted in terms of spatial and temporal coverage. In addition to surface measurements, model simulations play an indispensable role in the estimation of the aerosol radiative effect at the global scale and excel in predicting past or future trends of ADRF (Chang and Liao, 2009; Qiu et al., 201~~6~~7). Meanwhile, model simulations are subject to large uncertainties in terms of emissions, transport, and physical and chemical parametrization schemes (José A. et al., 2013).

Compared to the above methods, satellite remote sensing has an outstanding advantage of delivering aerosol information with high<u>er</u> spatial resolution and ~~continuous temporal~~ <u>larger spatial</u> coverage. Using solely satellite data or a combination with model simulations and observations constraint, many methods have been developed to retrieve global and regional ADRF estimates (e.g., Yu et al., 2004; Bellouin et al., 2005; <u>De</u> Graaf et al., 2013). However, these studies have mainly concentrated

70 on the top-of-atmosphere (TOA) radiation budget. Thus far, long-term estimates of the surface ADRF distribution have rarely been addressed~~, especially in China, one of the most populated and polluted regions globally~~ and few studies gave a full picture of surface ADRF over land (e.g.: Thomas et al., 2013; Chung et al., 2016). This lack of research is because satellites are unable to measure surface-level radiative fluxes directly. Furthermore, the retrieval of aerosol microphysical parameters remains challenging ~~are crucial in ADRF simulation~~, including single scattering albedo (SSA, see Table 1 for the acronyms) and ~~the~~

75 asymmetry parameter (ASY)~~, but their retrieval remains challenging~~. Many attempts have been made to solve this key problem. For instance, Thomas et al. (2013) adopted prescribed aerosol properties from the literature to estimate surface ADRF. Fu et al. (2017) took aerosol optical parameters from some AERONET ~~station~~sites as representative of the entire region to conduct grid-cell ADRF simulations. Undoubtedly, additional uncertainty ~~was~~ is introduced by the assumption of aerosol optical representativeness in the temporal and spatial dimensions. Some studies also nudged global model simulations towards

80 AERONET SSA to obtain the aerosol parameters (Chung et al., 2016). With the rapid development of satellite technology, more satellites are providing more detailed aerosol optical products via instruments such as the Polarization and Directionality of the Earth's Reflectance instrument (POLDER), and the Ozone Monitoring Instrument (OMI) (Levelt, et al., 2006; Tilstra and Stammes, et al., 2007). However, the accuracy of the SSA and ASY products over China ~~is~~ still ~~undesirable~~ needs to be improved (Oikawa et al., 2013; Dubovik, et al., 2019). Recently, using satellite and observational data assimilated into the

85 Goddard Earth Observing System, version 5 (GEOS-5), the National Aeronautics and Space Administration (NASA) has extended the Modern-Era Retrospective Analysis for Research and Application, version 2 (MERRA-2). Compared with its predecessor (MERRA-1), MERRA-2 offers important improvements in aerosol assimilations (Gelaro et al., 2017). The new dataset has the potential to provide improved estimates of aerosol microphysical parameters, such as SSA, and can be further used in the ADRF estimation. After SSA is determined, ASY, the only unknow model input~~s~~, can be retrieved by matching

90 the simulated radiative fluxes with satellite measurements from Clouds and the Earth's Radiant Energy System (CERES). Overall, based on the satellite and reanalysis datasets, including MERRA-2, the MODerate Resolution Imaging Spectroradiometer (MODIS) and CERES, the objective of this study is to ~~propose~~ provide quantitative estimates of fine-resolution ADRF distributions ~~in~~under the clear sk~~y~~ies using a radiative transfer ~~model. Here,~~model over East China (114°-124°E, 24°-38°N, shown in the Figure 1)~~. was taken as the validation area of ADRF retrieval, and the simulated radiative~~

95 ~~fluxes were compared with surface radiation measurements in East China.~~ Additionally, the aerosol vertical profiles in each grid, which were not considered in previous studies, are used to obtain more accurate ADRF. In our study, aerosol vertical profiles are determined by the Weather Research and Forecasting Model (WRF, version 3.2.1) and the National Centers for Environmental Prediction-Final Operational Global Analysis (NCEP-FNL). The detailed algorithm of aerosol profiles can be found in Section 2. ~~The~~ Other data acquisition is also presented in Section 2, and Section 3 introduces the method of ADRF

100 simulations. Section 4 includ~~ing~~es the retrieval of aerosol optical properties, validation of surface radiative fluxes with pyranometers, and detailed discussion of the error sources. Then this method ~~was~~is applied in each grid of East China during 2000-2016, and the uncertainty in the retrieval method is also discussed in Section 4. The conclusion is presented in Section 5.

2 Data

105 To acquire ADRF, the inputs (aerosol optical depth (AOD), SSA, ASY, albedo, etc.) to the radiative transfer model were determined from a combination of satellite and reanalysis datasets. AOD was derived from Collection 6 (C6) of MODIS Level 2 products over land (10-km resolution at the nadir) from the Terra satellite (Levy et al., 2013). Compared with C5, MODIS C6 mainly updated the cloud mask to allow heavy smoke retrievals and fine-tuned the assignments for aerosol types as function of season and location over the land. Levy et al. (2013) made a comparison between MODIS C5, C6 and AERONET, and

110 found that the correlation coefficient of C6/AERONET increases slightly, and the slope and offset of the regression curve only changed slightly compared with C5/AERONET. MODIS /AOD retrieval primarily employs three spectral channels, centered at 0.47, 0.66, and 2.1 μm and is interpolated at 0.55 μm (Kaufman et al., 1997). Li et al. (2003) demonstrated that the MODIS /AOD Level 2 product is appropriate in eastern China and exhibits high precision. In addition, He et al. (2010) found that MODIS /AOD was highly correlated with sunphotometer (CE318) measurements at 7 sites in the Yangtze River Delta (YRD)

115 region (118°-123°E, 29°-33°N), with a correlation coefficient of 0.85 and with 90% of cases falling in the range of ΔAOD = ± 0.05 ± 0.20 AOD (Chu et al., 2002). Thus, the uncertainty in the AOD is regarded as 20% in this study.

HThe hourly SSA product was provided by MERRA-2. was estimated by the ratio of total aerosol scattering aerosol optical thickness (AOT) to total aerosol extinction AOT at a wavelength of 0.55 μm. MERRA-2 combines GEOS-5 and the three-dimensional variational data assimilation (3DVar) Gridpoint Statistical Interpolation analysis system (GSI). GEOS-5 is

120 coupled to the Goddard Chemistry, Aerosol, Radiation and Transport (GOCART) aerosol module, which includes five particulate species (sulfate, dust, sea salt, organic and black carbon) (Colarco et al., 2010). The optical properties of these aerosols are primarily from the Optical Properties of Aerosols and Clouds (OPAC) dataset (Hess et al., 1998), in which aerosol optical parameters are calculated based on the microphysical data (size distribution and spectral refractive index) under the assumption of spherical particles and they are given for up to 61 wavelengths between 0.25 and 40 μm (Hess et al., 1998).the

125 SSA value at 0.55 μm can be interpolated at the other wavelengths. MERRA-2 provides SSA data at 0.55 μm. It is calculated by the ratio of total aerosol scattering aerosol optical thickness (AOT) to total aerosol extinction AOT at 0.55 μm, and these two are the outputs of GOCART model (Colarco et al., 2010). More details of the aerosol module in MERRA-2 can be found in Randles et al. (2017) and Buchard et al. (2017). The new dataset has been used in many recent studies and is appropriate for environmental and atmospheric research (Song et al., 2018). The input SSA was interpolated to other wavelength in SBDART,

130 which will be discussed detailly in the Methodology (Section 3).

The upward radiative flux at TOA was used to constrain and determine the ASY. The shortwave (SW, 0.3-5 μm) TOA flux was acquired by CERES Single Scanner Footprint (SSF) level 2 product from Terra satellite. CERES SSF measures the instantaneous reflected SW radiance under clear-sky conditions. To convert from radiance to flux, angular distribution models (ADM) were used in the CERES SSF product (Loeb et al., 2003). The CERES file contains one hour of data, and the CERES

135 SSF footprint nadir resolution is approximately 20 km. According to Su et al. (2015), the uncertainty of TOA SW flux is 1.6% over clear land.

Another important parameter for ADRF simulations is the surface albedo, and it was derived from ~~The black-sky albedo, derived from the~~ daily MODIS MCD43C3 black-sky ~~SW~~ albedo product (C6)~~, was used in this study~~. Surface albedo product includes seven narrow bands and three broadbands (visible (0.3-0.7μm), near-infrared (0.7-5.0μm), and SW (0.3-5μm))~~ are included in this product. Here, albedo product in SW band was used in our study.~~ Each file contains 16 days of combined Level 3 data from the satellites Aqua and Terra, with a spatial resolution of 0.05~~2~°. It also contains the data quality information, that is, the proportion of inversion retrieval information in each pixel. For example, data quality index 0 represents the best quality (100% with full inversion and no fill values), this index increases with the decrease of the proportion of inversion retrieval pixel, and 4 represents 50% or less fill values. Notably, to ensure accuracy, only the albedo values with ~~a~~ high ~~confidence~~ quality index (0-4) ~~index~~ were used. The uncertainty in the high-quality MODIS albedo is less than 5% (Cescatti et al., 2012).

The total column ozone, total column water vapor and atmospheric profile data were from the ERA-Interim (European Center for Medium-Range Weather Forecast (EC~~W~~M~~W~~F) Interim Reanalysis). Specifically, the atmospheric profile includes the altitude, temperature, water vapor density, and ozone density at 37 pressure levels (1, 2, 3, 5, 7, 10, 20, 30, 50, 70, 100 to 250 at 25-hPa intervals, 300 to 750 at 50-hPa intervals, and 775 to 1000 at 25-hPa intervals). The data quality of the ERA-Interim reanalysis data can be found in Dee et al. (2011).

The aerosol vertical profile plays a non-negligible role in aerosol radiative forcing. ~~Here, the aerosol vertical profile model retrieved by He et al. (2016) was applied in each grid to take the place of the default in the radiative model. The retrieval can be briefly described as follows. Based on the two-layer aerosol model, two crucial parameters of the aerosol vertical profile are the planet boundary layer height (PBL) and the aerosol layer height (ALH) (He et al.,2008). The aerosol extinction coefficient is assumed to decrease exponentially with altitude above the top of the PBL, and the~~ In SBDART, aerosol vertical profile is shaped by aerosol density and the according altitude. The aerosol density is a proportion of AOD in different altitude, and the overall profile is scaled by AOD. The aerosol density is set to fall exponentially between two altitudes by default. In our study, aerosol vertical profile in SBDART was derived from two-layer aerosol vertical distribution model, which is proposed by He et al. (2008). In this two-layer aerosol model (Figure S1), aerosol extinction coefficient is assumed to decrease exponentially with altitude above the top of the planet boundary layer (PBL) and the extinction coefficient keeps uniform below the PBL. Based on this aerosol model, two inputs of aerosol vertical profile need to be determined, PBL and aerosol layer height (ALH). ALH is defined as the level where the aerosol extinction coefficient decreases to 1/e (scaling height) of that at the top of the PBL. PBL and ALH input to SBDART along with the according aerosol density. In this study, ~~The~~ PBL was simulated using a three-domain, two-way nested simulation of the WRF Model (~~Weather Research and Forecasting Model,~~ version 3.2.1). ALH can be influenced by the transport of air mass and the convective dispersion of aerosols, both of which are usually associated with large-scale weather systems. Based on the different meteorological conditions, an automated workflow algorithm of ALH was constructed, and ALH was estimated by the meteorological parameters (relative humidity, temperature, wind speed and wind direction) from ~~the National Centers for Environmental Prediction Final Operational Global Analysis (NCEP-FNL) via an automated workflow algorithm~~. The detailed algorithm and the according calculations of PBL

11

and ALH retrieval can be found in the He et al. (2016). The aerosol profiles were utilized to calculate the surface-level visibility from AOD, and the long-term spatial comparison with surface measurements over East China displayed that 90% of the samples exhibited correlation coefficients greater than 0.6 and that 68% of the samples exhibited correlation coefficients greater than 0.7 (He et al., 2016).

175 All of these multiplatform datasets with their spatial and temporal resolutions were are summarized in Table 2. In this study, bilinear interpolation was used in these datasets, and these datasets were interpolated to a spatial resolution of 0.1°×0.1° to collocate with the MODIS/AOD data. Additionally, tThe ADRF simulation was also performed in each 0.1°×0.1° grid over East China. For temporal resolution, AOD and TOA radiation fluxes were from the MODIS and CERES sensor aboard the Terra satellite respectively, and they are available once per day. Both SSA and ERA-Interim are hourly means, surface albedo 180 product in daily means. The ADRF simulations were only performed at the passing over of the Terra satellite under clear skies. The temporal coverage is from 2000 to 2016. The research area and surface measurement sites for validation are shown in Figure 1.

3 Methodology

Clear-sky ADRF in the SW (0.25-4 μm) spectral region was simulated by the Santa Barbara Discrete Atmospheric Radiative 185 Transfer (SBDART) model (Ricchiazzi et al., 1998). This model has been widely adopted for the estimation of aerosol radiative forcing and validated with high accuracy (Li et al., 2010). In this study, SBDART model was used to estimate broadband SW (0.25-4 μm) surface irradiances and ADRF over East China. It is on the basis of the DISORT radiative transfer model, the low-resolution band models developed for LOWTRAN 7 atmospheric transmission, and the Mie scattering results for light scattering by water droplets and ice crystals (Ricchiazzi et al., 1998). Here, LOWTRAN 7 (Low Resolution Atmospheric 190 Transmittance 7) solar spectrum was adopted in SBDART. This radiative transfer model also includes the standard aerosol models derived from Shettle and Fenn (1975), in which aerosol optical parameters are wavelength dependence and the scattering parameters depend on the surface relative humidity. Users can also define different aerosol parameters in different wavelength. The default of the according spectral information is interpolated/extrapolated to all wavelengths using linear fitting on SSA/ASY, and using Ångstrom coefficients on AOD. According to Wang, P. et al. (2009), the input of aerosol parameters 195 has very minor effect on the accuracy of irradiance simulation when using spectrally averaged values compared with detail spectral information. Therefore, aerosol parameters (AOD, SSA, ASY) at 0.55 μm were used in the radiative transfer model. As for surface albedo, it is simply assumed that angular distribution of surface-reflected radiation is completely isotropic in the model. In our study, MODIS SW MCD43C3 (0.3-5 μm) product is used as albedo input, and it is nearly consistent with wavelength coverage (0.25-4 μm) of the output surface irradiances in SBDART.

200 As shown in Figure 2, the main inputs of the SBDART model include aerosol properties (AOD from MODIS; SSA from MERRA-2; ASY from the retrieval (Section 4.2)), surface albedo (from MODIS), aerosol vertical profile (from NCEP), atmospheric profiles (from ECWMWF), total column ozone and water vapor (from ECWMWF). The main outputs are

12

radiative fluxes at the surface and TOA with and without aerosols. ADRF is defined as the difference in net radiative flux (downward minus upward) between aerosol and no-aerosol conditions. Here, we mainly concentrated on ADRF at the surface:

205
$$\text{ADRF}_{sur} = (F\downarrow - F\uparrow) - (F_0\downarrow - F_0\uparrow), \tag{1}$$

where F and F_0 represent radiative fluxes with and without the aerosol at the surface, respectively. The upward and downward arrows denote the directions of the radiative fluxes, which can be obtained by the outputs of SBDART. For simplicity, the upward radiative fluxes at the TOA are called F_u_toa, and the downward/upward radiative fluxes at the surface are called F_d_sur and F_u_sur, respectively (see Table 1 for the acronyms).

210 Besides above, Mann-Kendell (MK) test (Mann, 1945; Kendall, 1975) was used to calculate the trend of ADRF time series and its significance level (above 90%) in our study. It identifies that whether monotonic trends exist in a time series and is widely employed for trend analysis of aerosol data. The detailed analysis produce can be found in Li et al. (2014). Prior to trend analysis, ADRF data were deseasonalized by subtracting the monthly mean during 2000-2016 to eliminate the influence of annual and seasonal cycles.

215 **4 Results and discussion**

4.1 Retrieval of aerosol properties

Before ADRF simulation, ~~one of the inputs, SSA from~~ the accuracy of MERRA-2 SSA product, was evaluated firstly. In East China, six ~~three~~ sunphotometer sites, ~~Pudong (121.79ºE, 31.05ºN), Taihu (120.22ºE, 31.42ºN), and~~ Xuzhou (117.14ºE, 34.22ºN), Shouxian (116.78ºE, 32.56ºN), Hefei (117.16ºE, 31.91ºN), Taihu (120.22ºE, 31.42ºN), Pudong (121.79ºE, 31.05ºN)
220 and Hangzhou (120.16ºE, 30.29ºN) (Figure 3a), were chosen for comparison with MERRA-2 SSA data. ~~due to their large available samples, while other sites in East China did not have enough data for analysis. The blue triangles in Figure 1 represent t~~ The location of the sunphotometers was shown in Figure 3(a), and ~~he locations of the sunphotometers, and~~ their geographical characteristics, ~~and~~ observing~~ation~~ periods, sample numbers as well as the fitted regression equation between MERRA-2 and sunphotometer SSA were presented in Table 3.~~can be found in Table 3~~. Five sites (Xuzhou, Shouxian, Hefei, Taihu and
225 Hangzhou)~~Taihu and Xuzhou~~ are AERONET sites and Level 1.5 inversion data of ~~in~~ AERONET ~~sites~~ were used. The uncertainty ~~in the~~of AERONET products can be found in Dubovik and King (2000). Another sunphotometer (CE318, Cimel Electronique, France) in Pudong was ~~is~~ calibrated annually and maintained routinely, and a detailed description of calibration was presented in Cheng et al. (2015). The sunphotometer spectral products are available at wavelengths of 440, 675, 870, and 1020 nm, and they were interpolated at 0.55 μm to match MERRA-2 SSA. The collection time was constrained from 09:00 to
230 14:00 (local time), covering the overpass time of the Terra satellite. Meanwhile, the relatively high solar zenith in this period avoids possible inversion errors and improves the data accuracy (Tian et al., 2018b). Additionally, the specific MERRA-2 grid cell containing the sunphotometer was selected, and ~~the~~ sunphotometer SSA was hourly averaged to match the MERRA-2 SSA product. ~~Figure 3 displays the detailed comparisons at Pudong, Taihu, and Xuzhou. The blue solid line represents the fitting curve of the scatter dots, and the dashed lines are the range of ±10% relative error.~~The detailed comparisons at Xuzhou,

13

235   Shouxian and Hefei were shown in Figure 3b. Orange dots represent Xuzhou samples and orange line is the according fitting curve, while the green represents Shouxian, and the black is Hefei. Figure 3c displays the comparison results at Taihu, Pudong and Hangzhou. Red denotes Taihu, the purple is Pudong and the yellow is Hangzhou. As shown in Figure 3, dashed lines are the range of ±10% relative error, ~~A~~all samples in Taihu~~, and~~ Pudong, Hefei, ~~and~~ 94% of samples in Xuzhou, 93% in Shouxian and 98% in Hangzhou fall within the ±10% error. This finding suggests that MERRA-2 SSA agrees well with the

240   sunphotometer data, even though few SSA samples ~~some dots in Xuzhou~~ are beyond the error range. ~~The further comparison between MERRA-2 SSA and sunphotometer are shown in Figure S1 (Supplementary Information). The boxplots for the three sites indicates the mean value of MERRA-2 SSA is similar to previous measurements in East China, such as Shanghai (0.91), Taihu (0.91) and Huainan (0.89), (Liu et al.,2012; Che et al.,2017; Che et al., 2019).~~ Furthermore, the slopes of linear fitting curve are less than 1 at all sites except Shouxian (Table 3), and it ~~also~~ reveals that MERRA-2 SSA has systematic biases at

245   most area of East China~~generally produces lower SSA than surface measurements in Taihu and Xuzhou~~. The primary reason for the discrepancy ~~between MERRA-2 and surface measurements~~ is the simple aerosol model assumption in MERRA-2 (Buchard et al., 201~~7~~8). Only five aerosol types (sulfate, dust, sea salt, organic and black carbon) are involved; the lack of nitrate aerosols, which are highly scattering aerosols, may result in ~~is responsible for~~ the underestimation of MERRA-2 SSA~~, especially in Xuzhou, with various aerosol sources related to human activities (Che et al., 2015)~~. In addition, the calibration

250   errors among the~~se~~ ~~three~~ instruments should be considered. Generally, the evaluation results in six ~~three~~ sites show that the accuracy of MERRA-2 SSA product is acceptable in East China, with ±10% uncertainty.

After SSA was determined, ASY is the only unknown ~~model~~ input parameter. ASY is the key to portraying the scattering direction of aerosols. ASY=1 denotes completely forward scattering, and ASY=0 is symmetric (Rayleigh) scattering. Here, gridded ASY was simulated by matching observed F_u_toa (from CERES) with simulated F_u_toa (from SBDART). The

255   sensitivity test indicates that F_u_toa, just similar with ~~like~~ F_u_sur (shown in Figure S3b~~7b~~), is a monotonically increasing function of ASY with other fixed inputs. Consequently, only one F_u_toa can be obtained by one specific ASY. In this premise, a binary search was applied to approximate ASY to improve calculation efficiency (Chang, 2013). The goal of the binary search is to find the ASY when the simulated F_u_toa is close to the observed F_u_toa. To accomplish this, the ranges of F_u_toa are repeatedly diminished by taking the middle ASY as one of the boundary values, and when the difference between

260   the F_u_toa observed by CERES and calculated by SBDART is less than 1, the corresponding approximation of ASY is finally obtained. The detailed scheme is illustrated in Figure 4. First, the value for ASY is initially assumed in the reasonable range of 0.1-0.9, and the upper and lower boundaries of ASY, along with other parameters, are input to SBDART to yield the initial range of calculated F_u_toa_a and F_u_toa_b. Then, this range is checked to determine whether it includes the F_u_toa (observed by CERES) by multiplying ((F_u_toa_a- F_u_toa)*(F_u_toa_b- F_u_toa)). If the multiplication result is negative,

265   meaning that ASY falls within this range (ASYa, ASYb), the average of F_u_toa_a and F_u_toa_b is set as a new boundary (F_u_toa_c). Otherwise, this case is discarded, and the retrieval is not continued (ASY=NaN), perhaps due to inappropriate inputs. Next, for cases in which the multiplication result is negative, the multiplication process is applied to the new boundary ((F_u_toa_a- F_u_toa)*(F_u_toa_c- F_u_toa)). If this multiplication result is negative, the ASY falls within this range (ASYa,

14

ASYc). Then, ASYc is set to represent ASYb. Otherwise, ASYc is set to represent ASYa. This process represents the scope-narrowing of the ASY boundary discussed above. With several iterations of narrowing the scope, the boundaries of the simulated F_u_toa become close to the true value of F_u_toa (observed by CERES). When the difference between the simulated F_u_toa boundary and the observed F_u_toa is less than 1, the corresponding ASY is considered as one approximation. In this process, the input parameters, including AOD (from MODIS), SSA (from MERRA-2), surface albedo (from MODIS), aerosol vertical profile (from NCEP), atmospheric profiles (from ECWMWF), total column ozone and water vapor (from ECWMWF), were input into the SBDART model together in every iteration. All these inputs from 2000-2016 were used to simulate ADRF in each grid of East China. All calculations were performed on the Linux system. Following this method, ASY was retrieved in each grid cell over East China. The range of retrieved ASY is 0.50-0.80, and the mean ASY is 0.63, which is consistent with the observation site (Taihu) in East China (Xia et al., 2007). According to Mie theory, ASY is determined by the size distribution and the complex refractive index of aerosols. Therefore, the difference of ASY in East China can be partly related with the difference of fine mode radius. Xia et al. (2007) has reported that the fine mode volume median radius at Taihu site averages 0.181 μm over a range of AOD from 0.6-1.0, while it is 0.168 μm in northern China. In ASY retrieval, ASY is assumed to vary enough to match F_u_toa with ensuring the accuracy of all other inputs (e.g. AOD, SSA). This assumption can deviate from the reality if there are obvious differences between real and retrieval values of other inputs. This above condition can easily occur in the process of ASY retrieval, when ASY cannot be retrieved (ASY=NaN). Even if ASY can be obtained, ASY can be inaccurate when other inputs have large biases. The uncertainty of ASY caused by the other inputs (AOD, SSA, albedo, CERES F_u_toa) will be quantified in the following uncertainty analysis (Section 4.3). After aerosol optical properties were obtained, these parameters from multiplatform datasets can be input into the SBDART model to simulate surface radiative fluxes and ADRF in East China according to the methodology in Section 3.

4.2 Validation of the method

Before conducting ADRF simulation in each grid of East China during 2000-2016, this method was first to applied in the single three grids of selected sites to assess the performance of ADRF retrieval. Three radiation sites stations in Baoshan (121.45°E, 31.4°N), Fuzhou (119.29°E, 26.08°N), Yong'an (117.37°E, 25.98°N) wereas chosen to make the comparisons between calculated F_d_sur and surface observation by the pyranometers (FS-S6, China) during 2014-2016. Red circles in Figure 1 denote the specific locations of pyranometers. Their geographical characteristics and observing periods are listed in Table 3. Baoshan and Fuzhou are urban and coastal sites while Yong'an represents suburb and inland sites. The different aerosol concentration levels and abundant aerosol types in these sites can represent the most of aerosol properties in East China. These pyranometers had regular maintenance and were calibrated annually through intercomparisons with the basic reference station. Additionally, quality control has been performed at these sites according to Long and Shi (2008), including the removal of physical possible limits as determined by Baseline Surface Radiation Network (BSRN) and use of configurable limits based on climatological analysis of measurement data. The uncertainty in the pyranometers is expected to be 5% (Song,

2013). Simulated F_d_sur was averaged in the scope of a 40 km side length with the center at the pyranometer, and the measured F_d_sur was averaged within ±30 min of the satellite overpass (Ichoku, et al., 2002).

Figure 5 displays the comparison results between simulated F_d_sur and observed F_d_sur by pyranometers at ~~the~~ three sites. The simulated F_d_sur is fairly consistent with the observations, with correlation coefficients of 0.87 in Baoshan (Figure 5a) and Fuzhou (Figure 5b) and 0.90 in Yong'an (Figure 5c). Root mean squared error (RMSE) is a good indicator for measuring the discrepancy between observed and simulated F_d_sur data. The RMSE is 7.9 W m^{-2} in Baoshan, 7.5 W m^{-2} in Fuzhou and 5.6 W m^{-2} in Yong'an. This discrepancy only accounts for 3-5% of ~~the~~ ADRF, indicating that this retrieval method has a relatively higher accuracy than those in other studies (e.g., Thomas et al., 2013; Fu et al., 2017). Additionally, all slopes are less than 1, which implies that the method has systematic biases at these sites. ~~That is, the simulated F_d_sur is overestimated relative to observations in clear conditions but underestimated in polluted conditions. Thus, in very clear or polluted conditions, this method can smooth F_d_sur variations.~~ A similar tendency was found in the comparison between MODIS AOD and sunphotometers in East China by He et al. (2010); it is speculated ~~therefore,~~ the main systematic error in ~~the~~ ADRF simulation may come from the input, MODIS AOD. ~~Additionally, all intercepts of the fitting lines are greater than 0, indicating that the method can produce errors, especially in clear conditions.~~ Nevertheless, satisfactory comparison results indicate the suitability and feasibility of ADRF retrieval in the off/near the sea ~~southern~~ and urban/suburb ~~northern sites~~ sites of East China, although the type~~s~~ of underlying surface and aerosol properties~~sources~~ ~~in the north~~ are evidently different ~~from those in the south~~ in these areas.

To further assess the discrepancy between simulated F_d_sur and the observations, the relative errors of each case at the three sites were calculated. The results suggest that underestimated cases (negative relative errors) account for 61% of the total cases and overestimated cases (positive relative errors) account for 39%. According to the validation results, the sources of error in the simulation may be attributed to the following reasons:

Cloud contamination: An examination of cloudiness was carried out at the three sites. According to the empirical clear-sky detection method, one-hour radiation data of a pyranometer was used to discriminate clear-sky observations (Xia et al., 2007). The red dots in Figure 5 represent the cloudiness case detected by the pyranometer. Meanwhile, from the MODIS true color map composed by channels 1, 4 and 3 (not shown), the olive green dots denote the specific case in which the site is completely covered by clouds. Taking one olive green cases (Baoshan, October 18, 2014) for an example. As shown in the Figure S2, it is obvious that a large amount of cloud exists in the area of 29°N-31°N and 120°E-122°E, and Baoshan site is at the edge of the cloud. In this case, MODIS AOD was overestimated compared with sunphotometer AOD, this because some cloud effects were not completely removed from the MODIS/AOD calculation. Therefore, a~~A~~ large discrepancy can occur in these cases between simulated F_d_sur and observation ~~is also evidence of substantial errors produced by clouds~~. The cloud effect, especially ~~that of~~ residual thin cirrus clouds, is difficult to completely remove from MODIS AOD (Kaufman et al., 2005). Moreover, the cloud mask algorithm in MODIS aerosol inversion sometimes fails to distinguish fog or haze in high-humidity conditions. Many more fog days can be ~~are~~ observed in Fuzhou than ~~at~~ the other two sites, and fogginess can significantly

reduce the accuracy of the simulation (Ye et al. 2010). In addition, the error source of MODIS AOD is also from errors in the
335 aerosol model assumption and surface reflectivity (Xie et al., 2011).

Different spatial and temporal representativeness: In the validation, the area measurement (satellite and reanalysis data) was compared to point measurements (pyranometer). For temporal matching, the pyranometer can capture the process of perturbation induced by air mass movement within one hour, whereas satellite can only provide the instantaneous conditions. Hence, this comparison method inevitably introduces some degree of uncertainty.

340 **Instrument and radiative transfer errors:** One error source in pyranometers is the thermal offset effect. This spurious signal is due to the difference in temperature between the inner dome and the detector of a pyranometer and can lead to additional errors in the irradiance measurements, especially diffuse irradiance (Sanchez et al., 2015). To reduce this effect, a pyranometer should be installed in a transparent ventilation hood. Alternatively, several statistical methods have also been proposed to suppress the thermal offset effect (e.g., Song, 2013; Cheng et al., 2014). In this study, the correction of the thermal offset was
345 not performed because of the lack of additional observation data. Aside from the instrument error, the model simulation discrepancy also depends on the radiative transfer models. They are based on some simplifications, including the sphericity of aerosol particles and the directional reflectance of the surface. Derimian et al. (2016) found that neglecting aerosol particle nonsphericity can overestimate the aerosol cooling effect. Furthermore, simulation results vary slightly among different models due to their different assumptions in radiative transfer. For instance, Yu et al. (2007) compared three models (second simulation
350 of the satellite signal in the solar spectrum (6S), ModODerate resolution atmospheric TRANsmission Transmission (MODTRAN) and SBDART) at Xianghe station and showed that approximately 80% of the cases simulated by SBDART were lower than the surface observations, while the 6S simulation results were higher.

~~**The effect of aerosol sources:** The Hybrid Single Particle Lagrangian Integrated Trajectory (HYSPLIT) model was employed for the backward trajectory of air mass (http://ready.arl.noaa.gov/HYSPLIT.php) to explore the effect of air mass origin on the~~
355 ~~ADRF simulation. Here, archive data from the Global Data Assimilation System (GDAS) were applied in this model. A 48 h backward trajectory of air mass ending at the three pyranometers at a height of 0.5 km was used to trace the origin of the surface-level air mass. In Fuzhou, almost all the directions of blue lines (Figure S2), which denote negative relative errors of simulation, are northward, while the directions of red lines with positive errors are southward. The major aerosols associated with the blue lines are inferred to be anthropogenic and high-scattering particles. MERRA-2 SSA is always underestimated in~~
360 ~~these conditions, potentially leading to the negative errors in the simulated F_d_sur because SSA has the same phase as F_d_sur (Figure 7a, shown below). Moreover, the direction of the air mass trajectory is found to be steady on consecutive days, and the change in the error sign is consistent with the change in the trajectory direction. Taking Yong'an as an example, three 48 h backward trajectories of air masses with negative errors all come from northeast during October 22-24, 2015 (Figure S3). This pattern is due to the similar aerosol types accompanying the same weather system over this region. In general, the aerosol~~
365 ~~source determines the dominant aerosol types and SSA, further producing additional uncertainty in the ADRF simulation.~~

4.3 Sensitivity test and uncertainty analysis

To determine the uncertainty of the method for ADRF simulation caused by each input parameter, a sensitivity test for input parameters was carried out. A specific case in Shanghai on October 11, 2015, was used with the following values: AOD = 0.62, SSA = 0.85, ASY = 0.69, surface albedo = 0.13, total column water vapor = 0.69 g/cm^2, and total column ozone = 0.28 atm-cm. Figure S3 portrays the responses of F_d_sur, F_u_sur and ADRF to changes in one parameter while holding the other parameters constant. To remove the impact of units, all the parameters are dimensionless; that is, the ratio of the input to the actual value is used as the x-axis value. The absolute value of every slope describes the impact of every parameter on the dependent variables (F_d_sur, F_u_sur and ADRF). Figure S3 presents the actual condition of this case when the value of the x-axis equals 1, in which F_d_sur is 629.15 W m^{-2}, F_u_sur is 83.52 W m^{-2}, and ADRF is -149.39 W m^{-2}. This situation denotes a strong cooling effect of aerosols at the surface. Apparently, different parameters impose diverse influences on the radiative values (F_d_sur, F_u_sur, and ADRF). As depicted in Figure S3, AOD, SSA, and ASY are three crucial parameters that greatly influence F_d_sur. Wang, P. et al. (2009) conducted the radiative closure experiment in the Netherlands and further found that, AOD can affect the changes of direct/diffuse irradiation, while SSA and ASY only affect the diffuse irradiance. For F_u_sur, albedo, AOD, and SSA are more important parameters. The impact of surface albedo is much larger than the others because albedo actually determines how much of the irradiance is reflected by the surface. For ADRF, SSA, AOD, and ASY are major factors in determining ADRF. Additionally, only a large AOD produces much cooler at the surface, whereas increases in SSA and ASY can result in decreases in the aerosol cooling effect. In general, sensitivity test shows that ADRF depends highly on AOD, SSA, ASY and albedo. Two parameters (atmospheric profile and aerosol vertical profile) are not discussed because these parameters have little impact on clear-sky ADRF in the above case. The atmospheric profile has a minor effect on the perturbations of ADRF compared with the total columns of atmospheric component (water vapor and ozone). This result has also been proven by Yu et al. (2007) and Li et al. (2016). As for aerosol profile, two typical shapes were input to SBDART for the sensitivity test. The first type (type I) has an elevated aerosol layer, and the second type (type II) is the two-layer aerosol model as mentioned above (Figure S1). The changes of the elevated layer height (type I) or PBL/ABL (type II) have very little impact on ADRF, and the according maximum value of ADRF difference only can reach 0.5 W m^{-2}. This conclusion is consistent with Guan et al. (2009). However, this impact becomes much stronger in the presence of absorbing aerosols, especially in some extreme cases such as dust storms and biomass burning (Wang and Christopher, 2006). Reddy et al. (2013) also demonstrated that surface aerosol radiative forcing can be enhanced by 25% due to the insertion of the extinction profile of absorbing aerosols to replace the default profile.

On the basis of these four high-sensitivity factors, the uncertainties in ASY and ADRF due to these parameters were quantitatively assessed. According to data uncertainty mentioned in Section 2 and the SSA validation, the relative errors of AOD, SSA, albedo, and CERES F_u_toa are 20%, 10%, 5% and 1.6%, respectively. This lower/upper limit of parameter errors was input to the ADRF calculation, and the associated uncertainty was calculated by the difference between the simulated radiative flux with parameter errors and without errors. Notably, the uncertainty analysis is based on extreme conditions, and

the associated errors are much larger than the actual values. As displayed in Table 4, the uncertainty in ASY induced by SSA can reach up to 23%, indicating that SSA is a decisive factor in ASY retrieval when using CERES F_u_toa constraint. SSA also has the largest effect in regulating aerosol radiative forcing, which is consistent with the research on dust aerosols by Huang et al. (2009). AOD contributes uncertainties of 3.7% in ASY and 15.4% in ADRF. Albedo introduces 1.7~3.7% uncertainty in ASY and approximately 3% in ADRF. The error of CERES product produces approximately 1.7% uncertainty in ASY and 1.5% in ADRF. The results of uncertainty analysis agree well with those of previous studies. For example, Xia et al. (2016) revealed that AOD and SSA together can account for 94% of surface ADRF. Zhuang et al. (2018) further noted that the error sources from the absorbing component of AOD and coarse-aerosol SSA contributed to the greater uncertainty in the ADRF. Therefore, improving the precision of the input parameter is helpful for obtaining reliable ADRF estimation. As Michalsky et al. (2006) demonstrated, when using high-quality measurements as inputs to model, the biases between modeled and measured irradiance can decrease to 1.9%. In addition to these factors, Wang and Martin (2007) also revealed the effects of aerosol hygroscopicity on the aerosol phase function and the increase in SSA with RH enhancement, suggesting that relative humidity (RH) is also closely related to ADRF.

4.43 Long-term ADRF retrieval in East China

The above evaluations show the method for ADRF simulation is feasible and high-accuracy in East China, thus this method was further applied in each grid cell of East China to obtain a full coverage of ADRF during from 2000-2016. Figure 6a outlines an overall picture of annual mean ADRF at the surface over East China during the past 17 years. It provides valuable information about aerosol radiative effect not only in the urban areas with intensive human activities, but also in the suburb with unavailable observational data. ADRFs in all grids are negative, ranging from -220 W m^{-2} to -20 W m^{-2}, implying that aerosols have cooling effect at the on surface over East China. The yearly mean ADRF is -100.21 W m^{-2}. The magnitude of ADRF is higher than most cities in the world, such as Spain (Esteve et al., 2014), Gasan (Kim et al., 2006) and Karachi (Alam et al., 2011). The main reason is that AOD in East China is much larger than these cities, since East China has experienced rapid urbanization and economic development in the past 17 years and AOD is much larger than these regions. For example, mean AOD in East China is 0.62 in this study during 2003-2011 while AOD is 0.19 in Spain during 2003-2011 (Esteve et al., 2014). Red area denotes the high absolute value of ADRF (Figure 6), which are found in the densely populated and industrialized areas, including the western Shandong Province, YRD and Poyang Lake Plain. Low value (blue area) is observed in the Southern part, such as Fujian and southern Zhejiang Province. Obvious difference of ADRF distributions is found between the northern and southern part of East China, and the magnitude of ADRF increases from South to North. This pattern is consistent with site observations in Che et al., (20189), in which surface ADRF ranges from -150 to -100 W m^{-2} in the northern sites of East China (Huainan and Hefei in Anhui Province) while ADRF ranges from -100 to -50 W m^{-2} in the southern sites of East China (Jiande, ChunAn and Tonglu in Zhejiang Province). To further explore this difference, East China was divided into two parts: the North and South, with the boundary of 30° N. The occurrence frequencies of annual ADRF for each grid cell in the North and South were calculated in the Figure S4. The occurrence frequency shows a broad range from -

300 W m^{-2} to 0 and the interval is 20 W m^{-2}. In the North, the largest proportion of ADRF, with the value of 76.47%, falls in the range of -100~-80 W m^{-2}, while the largest proportion (64.71%) of ADRF falls in the range of -60~-40 W m^{-2} in the South. The extreme value over -250 W m^{-2} may result from severe haze in the winter. Aerosol cooling radiative effect can sharply increase with large aerosol loadings. According to Yu et al. (2016b), surface ADRF can reach up to -263 W m^{-2} in the haze days, while in the non-haze days, it can decrease to -45 W m^{-2} in Beijing on January 2013. Usually in the heavy haze, the enhanced surface cooling, combined with atmosphere heating, can result in a more stable environment. It is unfavourable for the diffusion and dispersion of the aerosols, can further make air accumulation and enhance aerosol ADRF (Wu et al., 2016). Meanwhile, positive ADRF also found in few grid cells, although it is not shown in the Figure S4. This condition occurs over bright surface in East China especially with the abundance of absorbing aerosols (Sundström et al., 2015). ~~Red area denotes the high absolute value of ADRFs (Figure 6a), which are found in the densely populated and industrialized areas, including the western Shandong, YRD and Poyang Lake Plain. Low value (blue area) is observed in the Southern part, such as Fujian and southern Zhejiang.~~ According to the uncertainty analysis, ADRF is closely associated with the inputs (SSA and AOD). Based on this, comparison was conducted among the mean spatial distribution of ADRF, AOD and SSA during 2000-2016 (Figure 7). It is clear to see that ADRF pattern is very similar to the negative phase of AOD pattern, that is, the areas of high AOD have low ADRF. As for SSA, the higher value can be found in the South than the North, which indicating the aerosols in the South are generally more scattering than the North. Therefore, the large difference between North and South can be mainly attributed to the difference in AOD. The ~~This pattern is mainly attributed to the difference of~~ industry locations and topography between the North and South are obviously different. With the development of economy and urbanization, l~~L~~arge amounts of anthropogenic aerosols in the North ~~are highly scattering, they~~ can impose strong cooling radiative effect in the past two decades. It is worth noting that, although western Shandong has lower urbanization compared with YRD, aerosol ~~this~~ cooling effect in western Shandong is even larger than in YRD. This is because Yimeng mountain (these mentioned places are all shown in Figure 1) locate~~ds~~ in the middle of Shandong, ~~it~~ blocks the west flow, ~~and make~~ leading to the enhancement of the aerosol accumulations and high AOD near its western border (He et al., 2012b). Meanwhile, Shandong is also easily impacted by air pollution transported from North China. In addition, high absolute value of ADRF is also found in Poyang Lake in Jiangxi with abundance of anthropogenic aerosols, and these areas are surrounded by the mountains, the poor ventilation condition ~~leads to~~ makes aerosols enhanced. Compared with the North, the South is characterized by more extensive vegetation coverage and less human activities, ~~dominated natural aerosols~~and AOD is relatively lower in the South (Figure 7b) and aerosols have weaker cooling effect. ~~have weaker cooling effect. The ADRF distribution over East China is similar with AOD, which is presented in He et al. (2012b), that is, the areas of high AOD is corresponding to high value of ADRF. Meanwhile, ADRF also depends on the aerosol types. In some regions of East China with abundant of absorbing aerosols, the positive value of ADRF can occur especially in the bright surface (Sundström et al., 2015). In addition, the temporal variation of ADRF distributions further indicates it changes remarkably in East China over past decades, and the North experiences more notable changes of ADRF compared the South, which needs to be further identified and explored with additional measurements. Figure 6b displays the yearly regional mean changes of ADRF from 2000 to 2016 and the yearly mean ADRF~~

20

is -100.21 W m^{-2}. It reflects ADRF shows a fluctuation pattern, with the lowest, -121.78 W m^{-2} in 2013 and the highest, -93.87 W m^{-2} in 2009. The magnitude of ADRF is higher than the most cities in the world, such as Spain (Esteve et al., 2014), Gasan (Kim et al., 2006) and Karachi (Alam et al., 2011).

Apart from spatial changes, temporal changes of ADRF during 2000-2016 were also analysed. Figure 8 displays the time series of monthly mean ADRF and AOD. For comparison, blue line represents ADRF and red line denotes AOD. They both show a fluctuation pattern, and they have an obvious negative phase with the correlation coefficient of 0.72. It indicates that the temporal change of ADRF is mainly attributed to the change of AOD. MK trends of ADRF and AOD are both positive but insignificant at 90% confident level, showing AOD and ADRF did not change significantly during 2000-2016 in East China. Paulot et al. (2018) also proved this insignificant trend of ADRF in China based on chemical-climate models. About AOD, Zhang et al. (2017) found that AOD trend increases since 2000-2007 and then decreases in the eastern China based on satellite observations. It is well known that the changes of AOD is closely linked with the change of anthropogenic emissions, especially in the developing country. Che et al. (2019) calculated that SO_2 is the dominant anthropogenic emissions factors to AOD in China during past few decades. Furtherly, model simulations also indicate the changes of sulfate aerosols are the largest contributor to AOD and aerosol effect in China (Paulot et al., 2018). MK trends of monthly mean ADRF in each grid cell during 2000-2016 were also calculated (Figure 9). Hatched regions indicate those exceeding the 90% significance level. It can be found high positive trend in Anhui and Jiangxi, indicating the aerosol cooling effect is weaker in this region during 2000-2016. However, a few regions experience the stronger of this cooling effect, especially in the northeast and south area of Yimeng mountain in Shandong. In general, the changes of ADRF during the past 17 years are mainly due to the anthropogenic emissions in East China. In addition, Paulot et al. (2018) further pointed that there is a nonlinear relationship between anthropogenic emissions and AOD/ADRF when considering the mix and oxidation of different emissions.

In addition, aerosol cooling radiative effect can sharply increase with large aerosol loadings. According to Yu et al. (2016b), surface ADRF can reach up to -163 W m^{-2} in the haze days, while in the non-haze days, it can decrease to -45 W m^{-2} in Beijing on January 2013. Usually in the heavy haze, the enhanced surface cooling, with combining of atmosphere heating, can result in a more stable environment, which is unfavourable for the diffusion and dispersion of the aerosols and further exacerbates air pollution (Wu et al., 2019). Therefore, aerosol radiative feedback plays a vital role in the severe haze events in winter.

4.4 Sensitivity test and uncertainty analysis

To determine the uncertainty of the method for ADRF simulation caused by each input parameter, a sensitivity test for input parameters was carried out. A specific case in Shanghai on October 11, 2015, was used with the following values: AOD = 0.62, SSA = 0.85, ASY = 0.69, surface albedo = 0.13, total column water vapor = 0.69 g/cm^2, and total column ozone = 0.28 atm cm. Figure 7 portrays the responses of F_d_sur, F_u_sur and ADRF to changes in one parameter while holding the other parameters constant. To remove the impact of units, all the parameters are dimensionless; that is, the ratio of the input to the actual value is used as the x-axis value. The absolute value of every slope describes the impact of every parameter on the dependent variables (F_d_sur, F_u_sur and ADRF). Figure 7 presents the actual condition of this case when the value of the

x-axis equals 1, in which F_d_sur is 629.15 W m^{-2}, F_u_sur is 83.52 W m^{-2}, and ADRF is -149.39 W m^{-2}. This situation denotes a strong cooling effect of aerosols at the surface. Apparently, different parameters impose diverse influences on the radiative values (F_d_sur, F_u_sur, and ADRF). As depicted in Figure 7a, AOD, SSA, and ASY are three crucial parameters that greatly influence F_d_sur. For F_u_sur, albedo, AOD, and SSA are more important parameters (Figure 7b). The impact of surface albedo is much larger than the others because albedo actually determines how much of the irradiance is reflected by the surface. Figure 7c implies that SSA, AOD, and ASY are major factors in determining ADRF. Additionally, only a large AOD produces much cooler at the surface, whereas increases in SSA and ASY can result in decreases in the aerosol cooling effect. In general, sensitivity test shows that ADRF depends highly on AOD, SSA, ASY and albedo. Two parameters (atmospheric profile and aerosol vertical profile) are not discussed because these parameters have little impact on clear-sky ADRF in the above case. The atmospheric profile has a minor effect on the perturbations of ADRF compared with the total columns of atmospheric component (water vapor and ozone). This result has also been proven by Yu et al. (2007) and Li et al. (2016). The sensitivity test also shows that, with a fixed total column of AOD, clear sky ADRF is not sensitive to the shapes of aerosol profiles. However, this effect becomes much stronger in the presence of absorbing aerosols, especially in some extreme cases such as dust storms and biomass burning (Wang and Christopher, 2006; Guan et al., 2009). Reddy et al. (2013) also demonstrated that surface aerosol radiative forcing can be enhanced by 25% due to the insertion of the extinction profile of absorbing aerosols to replace the default profile.

On the basis of these four high sensitivity factors, the uncertainties in ASY and ADRF due to these parameters were quantitatively assessed. According to data uncertainty mentioned in Section 2 and the validation result of SSA, the relative errors of AOD, SSA, albedo, and CERES F_u_toa are 20%, 10%, 5% and 1.6%, respectively. This lower/upper limit of parameter errors was input to the ADRF calculation, and the associated uncertainty was calculated by the difference between the simulated radiative flux with parameter errors and without errors. Notably, the uncertainty analysis is based on extreme conditions, and the associated values are much larger than the actual values. As displayed in Table 4, the uncertainty in ASY induced by SSA can reach up to 23%, indicating that SSA is a decisive factor in ASY retrieval when using the CERES F_u_toa constraint. SSA also has the largest effect in regulating aerosol radiative forcing, which is consistent with the research on dust aerosols by Huang et al. (2009). AOD contributes uncertainties of 3.7% in ASY and 15.4% in ADRF. Albedo introduces 1.7~3.7% uncertainty in ASY and approximately 3% in ADRF. The error of the CERES product produces approximately 1.7% uncertainty in ASY and 1.5% in ADRF. The results of the uncertainty analysis are similar to those of previous studies. For example, Xia et al. (2016) revealed that AOD and SSA together can account for 94% of the surface ADRF. Zhuang et al. (2018) further noted that the error sources from the absorbing component of AOD and coarse-aerosol SSA contributed to the greater uncertainty in the ADRF. Therefore, improving the precision of the input parameter is helpful for obtaining reliable ADRF estimation, especially in the surface (Wang, P., et al.,2009). As Michalsky et al. (2006) demonstrated, when using high-quality measurements as inputs to model, the biases between modeled and measured irradiance can decrease to 1.9%. In addition to these factors, Wang and Martin (2007) also revealed the effects of aerosol hygroscopicity on the aerosol phase function and the increase in SSA with RH enhancement, suggesting that relative humidity (RH) is also closely related to ADRF.

22

5 Conclusion

In this study, based on multiplatform datasets, high-accuracy ADRF distributions over East China during 2000-2016 were

535 portrayed ~~determined~~. MERRA-2 SSA data were first compared with sunphotometer data (Taihu, Xuzhou, Pudong), and the validation result shows that the relative error of the MERRA-2 SSA is ±10% over East China. Then, ASY in each grid was retrieved by matching the simulated F_u_toa by SBDART with satellite observations. ~~based on the CERES product. A binary search was used in ASY retrieval to improve the retrieval efficiency.~~ Then, aerosol optical properties (AOD from MODIS, SSA from MERRA-2, and ASY from the retrieval), surface albedo (from MODIS), aerosol vertical profile (from NCEP),

540 atmospheric profiles (from EC~~W~~M~~W~~F), total column ozone and water vapor (from EC~~W~~M~~W~~F) served as input parameters for SBDART to simulate ADRF in each grid cell of East China during 2000-2016.

The validation result of this method at three sites (Baoshan, Fuzhou, and Yong'an) reveals that simulated F_d_sur is highly correlated with the pyranometer data during 2014-2016, with correlation coefficients of 0.87 in Baoshan and Fuzhou and 0.90 in Yong'an. The RMSEs are 7.9 W m^{-2} in Baoshan, 7.5 W m^{-2} in Fuzhou and 5.6 W m^{-2} in Yong'an~~,~~. It show~~ing~~ that ADRF

545 retrieval is ~~feasibile~~feasible and has high accuracy over East China. ~~Furthermore, the simulation is found to have systemic errors at all sites and that it is overestimated in clear conditions and underestimated in polluted conditions. This pattern is similar to the validation of MODIS AOD with sunphotometers over East China and indicates that the major error source in ADRF simulations possibly comes from MODIS AOD inversion.~~ In addition, associated factors, including cloud contamination, instrument and radiative transfer errors, as well as different spatial and temporal representativeness, were

550 confirmed to produce additional~~ly~~ uncertainty in ADRF simulations. ~~Further analysis of the air mass origin also demonstrates that ADRF is closely related to the aerosol types and SSA.~~ Sensitivity test shows that ADRF depends highly on AOD, SSA, ASY and albedo. Uncertainty analysis shows the uncertainty in ADRF retrieval induced by SSA is calculated 24% and that by AOD is 15.4%.

~~After validation this method in three sites,~~ Finally, ADRF simulation was conducted in each grid of East China during 2000-

555 2016. Long-term ADRF distribution~~s~~ over East China w~~ere~~as presented ~~portrayed~~ for the first time. ADRFs in all grids are negative, the range of ADRF is between -220 W m^{-2} and -20 W m^{-2}, implying that aerosols have cooling effect on surface over East China. ~~The yearly regional mean ADRF is -100.21 W m^{-2}. It reflects ADRF shows a fluctuation pattern, with the lowest, -121.78 W m^{-2} in 2013 and the highest, -93.87 W m^{-2} in 2009. The magnitude of ADRF is higher than the most cities in the world, such as Spain (Esteve et al., 2014), Gasan (Kim et al., 2006) and Karachi (Alam et al., 2011). Obvious difference of~~

560 ~~ADRF distributions is found between the northern and southern part of East China. ADRF distribution is similar to AOD pattern in East China presented in He et al. (2012b). This pattern is mainly attributed to the difference of industry locations and topography between the North and South. Finally, sensitivity test shows that ADRF depends highly on AOD, SSA, ASY and albedo. Uncertainty analysis shows the uncertainty in ADRF retrieval induced by SSA is calculated 24% and that by AOD is 15.4%.~~Aerosols are found to have stronger cooling effect in the North compared with the South. ADRF spatial pattern is

565 consistent with the negative phase of AOD pattern, and the temporal changes of ADRF also have a close relationship with

AOD. They indicate that the changes of ADRF in East China can mainly attributed to the changes of AOD. Furthermore, the spatiotemporal changes of AOD and ADRF are controlled by anthropogenic emissions, especially sulfate emissions in East China during past 17 years.

In summary, this study suggests that the method for ADRF retrieval is feasible in East China can be utilized over the areas
570 with large variations in aerosol loadings and surface properties. Especially in suburbs with no monitoring resources, our study offers valuable information of on the direct radiative impact of aerosols. It is noted that, in our study, ADRF was calculated during the time that satellite passes by rather than the whole day. Furthermore, aerosol optical parameters, including AOD and SSA, were considered only at 0.55 μm, and multi-wavelength of them can input to the radiative transfer model to improve the ADRF accuracy (Wang, P., et al., 2009). More additional observation data from the sites, are needed to further verify the
575 performance of the ADRF retrieval and constrain these multiplatform datasets to improve the ADRF accuracy. In addition, it is necessary to improve the satellite instruments and the retrieval algorithm of aerosol properties; more novel methods, such as machine learning, can be involved in the ADRF estimates (Yin, 2010; Yu and Song, 2013). In the future work, the aerosol-induced changes in the surface radiation under climate change and agricultural economic impact also will be studied. This work can will provide a deep understanding of aerosol radiative effects and is also helpful for aerosol modeling over East
580 China.

Data availability. AOD from MODIS is available at http://ladsweb.nascom.nasa.gov/data/search.html, albedo is also from MODIS (https://e4ftl01.cr.usgs.gov/MOTA/MCD43C3.006/). SSA from MERRA-2 is available at https://disc.gsfc.nasa.gov/daac-bin/FTPSubset2.pl. TOA flux is from CERES
585 (https://ceres.larc.nasa.gov/products.php?product=SSF-Level2). Atmospheric aerosol profile is retrieval from NCEP/NCAR (http://www.esrl.noaa.gov/psd/data/gridded/data.ncep.reanalysis.html). Total column ozone, total column water vapor and atmospheric profile are from ECWMWF (https://www.ecmwf.int/en/forecasts/datasets/reanalysis-datasets/era-interim). The SSA from AERONET sites are available at http://aeronet.gsfc.nasa.gov/. HYSPLIT trajectory and dispersion model is simulated at http://ready.arl.noaa.gov/HYSPLIT.php.
590

Competing interests. The authors declare that they have no conflict of interest.

Author contribution. Qianshan He and Yanyu Wang designed and conducted the research and analysis. Rui Lyu, Xie Xin and Tiantao Cheng contributed to data analysis and interpretation. Ze Meng contributed to revise the paper and improve the English
595 writing. Meijin Huang and Junshi Wu provided the surface measurements data. Haizhen Mu offered the computational resources. Qiu-Run Yu collected the reanalysis datasets. Yanyu Wang wrote the manuscript. All authors contributed to improve the manuscript.

24

References

Alam K., Trautmann T., and Blaschke T.: Aerosol optical properties and radiative forcing over mega-city Karachi. Atmospheric Research, 101(3):773-782, https://doi.org/10.1016/j.atmosres.2011.05.007, 2011.

Bellouin, N., Boucher, O., Haywood, J., and Reddy, M.: Global estimate of aerosol direct radiative forcing from satellite measurements, Nature, 438(7071), 1138-1141, https://doi.org/10.1038/nature04348,2005.

Buchard,V., Randles., C.A. Silva, A.M., Darmenov, A., Colarco, P. R., and Govindaraju, R.: The MERRA-2 aerosol reanalysis, 1980 onward. Part II: Evaluation and case studies, J. Clim., 30(17).6823, https://doi.org/10.1175/JCLI-D-16-0613.1, 2017.

Cescatti, A., Marcolla, B., Santhana Vannan, S.K., Pan, J.Y., Roman, M.O., Yang, X., Ciais, P,Cook, R., Law, B., Matteucci, G., Migliavacca, M., Moors, E., Richardson, A., Seufert, G., and Schaaf, C. : Intercomparison of MODIS albedo retrievals and in situ measurements across the global FLUXNET network, Remote Sens. Environ., 121, https://doi.org/10.1016/j.rse.2012.02.019, 2012.

Chameides, W., Yu, H., Liu, S., Bergin, M., Zhou, X., Mearns, L., Wang, G., Kiang, C., Saylor, R., Luo, C., and Huang, Y.: Case study of the effects of atmospheric aerosols and regional haze on agriculture: an opportunity to enhance crop yields in china through emission controls? Proc. Natl. Acad. Sci. U. S. A., 96(24), 13626-13633, https://doi.org/10.2307/121272, 1999.

Chang, Shi-Kuo.: Data structures and algorithms. Software Engineering and Knowledge Engineering. 13. Singapore: World Scientific. ISBN 978-981-238-348-8, 2003.

Chang, W., and Liao, H.: Anthropogenic direct radiative forcing of tropospheric ozone and aerosols from 1850 to 2000 estimated with IPCC AR5 emissions inventories, Atmos. Oce. Sci. Lett., 2 (4): 201–207, https://doi.org/10.1080/16742834.2009.11446804, 2009.

Che, H., Zhang, X., Chen, H., Damiri, B., and Zhou, T.: Instrument calibration and aerosol optical depth validation of the China aerosol remote sensing network, J. Geophys. Res. Atmos., 114(D3), D03206, https://doi.org/10.1029/2008jd011030, 2009.

Che, H., Zhang, X. Y., Xia, X., Goloub, P., Holben, B., Zhao, H., Wang, Y., Zhang, X. C., Wang, H., Blarel, L., Damiri, B., Zhang, R., Deng, X., Ma, Y., Wang, T., Geng, F., Qi, B., Zhu, J., Yu, J., Chen, Q., and Shi, G.: Ground based aerosol climatology of China: Aerosol optical depths from the China Aerosol Remote Sensing Network (CARSNET) 2002–2013, Atmos. Chem. Phys., 15, 7619–7652, https://doi.org/10.5194/acp-15-7619-2015, 2015.

Che, H., Qi, B., Zhao, H., Xia, X., Eck, T. F., Goloub, P., Dubovik, O., Estelles, V., Cuevas-Agulló, E., Blarel, L., Wu, Y., Zhu, J., Du, R., Wang, Y., Wang, H., Gui, K., Yu, J., Zheng, Y., Sun, T., Chen, Q., Shi, G., and Zhang, X.: Aerosol optical properties and direct radiative forcing based on measurements from the China Aerosol Remote Sensing Network (CARSNET) in eastern China, Atmos. Chem. Phys., 18, 405-425, https://doi.org/10.5194/acp-18-405-2018, 2018.

635   Che, H., Xia, X., Zhao, H., Dubovik, O., Holben, B. N., Goloub, P., Cuevas-Agulló, E., Estelles, V., Wang, Y., Zhu, J., Qi, B., Gong, W., Yang, H., Zhang, R., Yang, L., Chen, J., Wang, H., Zheng, Y., Gui, K., Zhang, X., and Zhang, X.: Spatial distribution of aerosol microphysical and optical properties and direct radiative effect from the China Aerosol Remote Sensing Network, Atmos. Chem. Phys. Discuss., https://doi.org/10.5194/acp-2019-405, in review, 2019.

Cheng, T., Xu, C., Duan, J., Wang, Y., Leng, C., Tao, J., Che, H., He, Q., Wu, Y., Zhang, R., Li, X., Chen, J., Kong, L., and

640   Y., X., Seasonal variation and difference of aerosol optical properties in columnar and surface atmospheres over Shanghai, Atmos. Environ., 123, 315-326, https://doi.org/10.1016/j.atmosenv.2015.05.029, 2015.

Cheng, X., Ding, L., Yang, Y., Bai, S., Zhou, H., Peng, J., Quan, J., and Song, J.: Correction methods for thermal offset errors in TBQ-2-B pyranometers, J. Trop. Meteoro., 20(4), 375-385, https://doi.org/10.16555/j.1006-8775.2014.04.011, 2014.

Chu, D. A., Kaufman, Y. J., Ichoku, C., Remer, L. A., Tanré, D., and Holben, B. N.: Validation of MODIS aerosol optical

645   depth retrieval over land, Geophys. Res. Lett., 29(12), 1617−1621, https://doi.org/10.1029/2001gl013205, 2002.

Chung, C. E., Chu, J. E., Lee, Y., Van Noije, T., Jeoung, H., Ha, K. J., and Marks, M.: Global fine-mode aerosol radiative effect as constrained by comprehensive observations, Atmos. Chem. Phys.,16(13), 8071-8080, https://doi.org/10.5194/acp-16-8071-2016,2016.

Colarco, P., Silva, A. D., Chin, M., Diehl, T.: Online simulations of global aerosol distributions in the NASA GEOS-4 model

650   and comparisons to satellite and ground-based aerosol optical depth, J. Geophys. Res. Atmos., 115(D14), https://doi.org/10.1029/2009JD012820, 2010.

Dee, D. P., Uppala, S. M., Simmons, A. J., Berrisford, P., Poli, P., Kobayashi, S. Andrae, U., Balmaseda, M. A., Balsamo, G., Bauer, P., Bechtold, P., Beljaars, A. C. M., van de Berg, L., Bidlot, J., Bormann, N., Delsol, C., Dragani, R., Fuentes, M., Geer, A. J., Haimberger, L., Healy, S. B., Hersbach, H., Hólm, E. V., Isaksen, L., Kållberg, P., Köhler, M., Matricardi, M., McNally,

655   A. P., Monge-Sanz, B. M., Morcrette, J.J., Park, B.K., Peubey, C., de Rosnay, P., Tavolato, C., Thépaut, J.-N., and Vitart, F.: The ERA‐Interim reanalysis: Configuration and performance of the data assimilation system, Q. J. R. Meteorol. Soc., 137(656), 553- https://doi.org/10.1002/qj.828, 2011.

De Graaf, M., Stammes., P., and Tilstra, L. G.: Quantification of the aerosol direct radiative effect from smoke over clouds using passive space-borne spectrometry, AIP Conference Proceedings 1531, 640, https://doi.org/10.1063/1.4804851, 2013.

660   Derimian, Y., Dubovik, O., Huang, X., Lapyonok, T., Litvinov, P., Kostinski, A. B., Dubuisson, P., and Ducos, F.: Comprehensive tool for calculation of radiative fluxes: illustration of shortwave aerosol radiative effect sensitivities to the details in aerosol and underlying surface characteristics, Atmos. Chem. Phys., 16(9), 5763-5780, https://doi.org/10.5194/acp-16-5763-2016, 2016.

Dubovik, O. and King, M.: A flexible inversion algorithm for retrieval of aerosol optical properties from Sun and sky radiance

665   measurements, J. Geophys. Res. Atmos.,105, 20673–20696, https://doi.org/10.1029/2000jd900282, 2000.

Dubovik, O., Z. Li, M.I. Mishchenko, D. Tanré, Y. Karol, B. Bojkov, B. Cairns, D.J. Diner, W.R. Espinosa, P. Goloub, X. Gu, O. Hasekamp, J. Hong, W. Hou, K.D. Knobelspiesse, J. Landgraf, L. Li, P. Litvinov, Y. Liu, A. Lopatin, T. Marbach, H. Maring, V. Martins, Y. Meijer, G. Milinevsky, S. Mukai, F. Parol, Y. Qiao, L. Remer, J. Rietjens, I. Sano, P. Stammes, S. Stamnes, X. Sun, P. Tabary, L.D. Travis, F. Waquet, F. Xu, C. Yan, and D. Yin: Polarimetric remote sensing of atmospheric

670   aerosols: instruments, methodologies, results, and perspectives, J. Quant. Spectrosc. Radiat. Transfer, 224, 474-511, https://doi.org/10.1016/j.jqsrt.2018.11.024, 2019.

Esteve A R, Estellés, V, Utrillas, María P, and Martínez-Lozano J.A.: Analysis of the aerosol radiative forcing over a Mediterranean urban coastal site. Atmos. Res., 137,195-204. http://dx.doi.org/10.1016/j.atmosres.2013.10.009, 2014.

Fu, Y., Zhu, J., Yang, Y., Yuan, R., Liu, G., Xian, T., and Liu, P.: Grid-cell aerosol direct shortwave radiative forcing calculated

675   using the SBDART model with MODIS and AERONET observations: an application in winter and summer in eastern China, Adv. Atmos. Sci., 34(8), 952-964, https://doi.org/10.1007/s00376-017-6226-z, 2017.

Gelaro, R., McCarty, W., Suarez, M. J., Todling, R., Molod, A., Takacs, L., Randles, C., Darmenov, A., Bosilovich, M., and Reichle, R.: The modern-era retrospective analysis for research and applications, version 2 (MERRA-2), J. Clim., 30(14), 5419-5454, https://doi.org/10.1016/10.1175/JCLI-D-16-0758.1, 2017.

680   Gong, F., Xin, J., Wang, S., Wang Y., and Zhang, T.: Anthropogenic aerosol optical and radiative properties in the typical urban/suburban regions in China, Atmos. Res., 197(15)177-187, https://doi.org/10.1016/j.atmosres.2017.07.002, 2017.

~~Graaf, M., Stammes., P., and Tilstra, L. G.: Quantification of the aerosol direct radiative effect from smoke over clouds using passive space-borne spectrometry, AIP Conference Proceedings 1531, 640, https://doi.org/10.1063/1.4804851, 2013.~~

Guan, H., Schmid, B., Bucholtz, A., and Bergstrom, R.: Sensitivity of shortwave radiative flux density, forcing, and heating

685   rate to the aerosol vertical profile, J. Geophys. Res. Atmos., 115, https://doi.org/10.1029/2009JD012907, 2010.

Haywood, J., and Boucher, O.: Estimates of the direct and indirect radiative forcing due to tropospheric aerosols: a review, Rev. Geophys., 38(4), 513, https://doi.org/10.1029/1999rg000078, 2000.

He, Q., Li, C., Mao, J., Lau, A., and Chu, D.: Analysis of aerosol vertical distribution and variability in Hong Kong, J. Geophys. Res., 113, D14211, https://doi.org/10.1029/2008JD009778, 2008.

690   He, Q., Li, C., Tang, X., Li, H., Geng, F., and Wu, Y.: Validation of MODIS derived aerosol optical depth over the Yangtze River Delta in China, Remote Sens. Environ. 114(8), 1649-1661, https://doi.org/10.1016/j.rse.2010.02.015, 2010.

He, Q., Li, C., Geng, F., Yang, H, Li, P., Li, T., Liu, D., and Pei, Z.: Aerosol optical properties retrieved from sun photometer measurements over Shanghai, China, J.Geophy. Res. Atmos., 117(D16), https://doi.org/10.1029/2011JD017220, 2012a.

He, Q., Li, C., Geng, F., Lei, Y., and Li, Y.: Study on long-term aerosol distribution over the land of East China using MODIS

695   data, Aerosol Air Qual. Res.12,300-315, https://doi.org/10.4209/aaqr.2011.11.0200, 2012b.

He, Q., Li, C., Geng, F., Zhou, G., Gao, W., Yu, W., Li, Z., and Du, M.: A parameterization scheme of aerosol vertical distribution for surface-level visibility retrieval from satellite remote sensing. Remote Sens. Environ., 181, 1-13, https://doi.org/10.1016/j.rse.2016.03.016, 2016.

Hess, M.: Optical properties of aerosols and clouds: the software package OPAC, Bull. Am. Meteorl. Soc., 79(5), 831-844.
700 https://doi.org/10.1175/1520-0477(1998)079<0831:OPOAAC>2.0.CO;2, 1998.

Holben, B. N., Tanré, D., Smirnov, A., Eck, T. F., Slutsker, I., Abuhassan, N., Newcomb, W. W., Schafer, S., Chatenet, B., Lavenu, F., Kaufman, Y., Vande, J., Setzer, A., Markham, B., Clark, D., Frouin, R., Halthore, R., Karneli, A., O'Neill, N., Pietras, C., Pinker, R., Voss, K., and Zibordi, G.: An emerging ground-based aerosol climatology: aerosol optical depth from AERONET, J. Geophys. Res. Atmos. 106(D11), 12067-12097, https://doi.org/10.1029/2001JD900014, 2001.

705 Huang, J., Fu, Q., Su, J., Tang, Q., Minnis, P., Hu, Y., Yi. Y, and Zhao. Q.: Taklimakan dust aerosol radiative heating derived from CALIPSO observations using the Fu-Liou radiation model with CERES constraints, Atmos. Chem. Phys., 9(12),4011-4021, https://doi.org/10.5194/acp-9-4011-2009, 2009.

Ichoku, C., Chu, D., Mattoo, S., Kaufman, Y., Remer, L. A , Tanré, D., Slutsker, I, and Holben N.: A spatio-temporal approach for global validation and analysis of MODIS aerosol products, Geophys. Res. Lett., 29(12), MOD1-1–MOD1-4,
710 https://doi.org/10.1029/2001GL013206，2002.

IPCC: Fifth Assessment Report: Climate Change 2013, Cambridge University Press, New York, NY, USA, 2013.

José A. Ruiz-Arias, Dudhia, J., Santos-Alamillos, F., and David Pozo-Vázquez.: Surface clear-sky shortwave radiative closure intercomparisons in the weather research and forecasting model, J. Geophys. Res. Atmos., 118(17), 9901-9913, https://doi.org/10.1002/jgrd.50770, 2013.

715 Kaufman, Y. J., Tanre, D. L., Remer, A., Vermote, E. F., Chu, A., and Holben, B. N.: Operational remote sensing of tropospheric aerosol over land from EOS moderate resolution imaging spectroradiometer, J. Geophys. Res., 102,17051–17067, https://doi.org/10.1029/96jd03988, 1997.

Kaufman, Y. J., Remer, L. A. , Tanre, D. , Li, R. R. , Kleidman, R. , Mattoo, S. , Levy, R., Eck, T. Holben, B., Ichoku, C., Martins, J., and Koren, I.: A critical examination of the residual cloud contamination and diurnal sampling effects on MODIS
720 estimates of aerosol over ocean, IEEE Trans. Geosci. Remote Sens., 43(12), 2886-2897, https://doi.org/10.1109/tgrs.2005.858430, 2005.

Kendall, M. G.: Rank Correlation Methods, Griffin, London, 1975.

Kim, J., Yoon S. C., Kim S. W., Brechtel, F., Jefferson, A., Dutton, E.G., Bower, K.N., Cliff, S. and Schauer., J.: Chemical apportionment of shortwave direct aerosol radiative forcing at the Gosan super-site, Korea during ACE-Asia. Atmospheric
725 Environment, 40(35):6718-6729. https://doi.org/10.1016/j.atmosenv.2006.06.007, 2006.

Levelt, P., G. van den Oord, M. Dobber, A. Malkki, H. Visser, J. de Vries, P. Stammes, J. Lundell, and H. Saari.:The Ozone Monitoring Instrument, IEEE Transactions on Geoscience and Remote Sensing 44 (5): 1093–1101. https://doi.org/10.1109/TGRS.2006.872333,.2006.

Levy, R. C., Mattoo, S., Munchak, L. A., Remer, L. A., Sayer, A. M., and Hsu, N.C.: The Collection 6 MODIS aerosol products

730 over land and ocean, Atmos. Meas. Tech. 6, 2989-3034, https://doi.org/10.5194/amtd-6-159-2013, 2013.

Li, J., Carlson, B. E., Dubovik, O., and Lacis, A. A.: Recent trends in aerosol optical properties derived from AERONET measurements, Atmos. Chem. Phys., 14, 12271–12289, https://doi.org/10.5194/acp-14-12271-2014,2014.

Loeb, N. G., Kato, L. S., Loukachine, K., and Manalo-Smith, N.: Angular distribution models for Top-of-Atmosphere radiative flux estimation from the Clouds and the Earth's Radiant Energy System instrument on the Terra satellite, Part I: Methodology,

735 J. Appl. Meteor., 42(4), 338., 22, 338–351, https://doi.org/10.1175/JTECH1712.1, 2003.

Long, C. N. and Shi, Y.: An automated quality assessment and control algorithm for surface radiation measurements, The Open Atmospheric Science Journal, 2, 23–37, https://doi.org/10.2174/1874282300802010023, 2008.

Li, C., Mao, J., Lau, A., Yuan, Z., Wang. M., and Liu, X.: Characteristics of distribution and seasonal variation of aerosol optical depth in Eastern China with MODIS products (in Chinese). Chin. Sci. Bull. 48(22),2488-2495,

740 https://doi.org/10.1360/03wd0224, 2003.

Li X., Sheng L., Liu, Q., Liu Y., and Wang L.: Error in calculation of surface radiation based on SBDART radiative transfer model (in Chinese), Period. Ocean Uni. Chin. 46(8), 13-18, 2016.

Li, Z., Lee, K., Wang, Y., Xin, J., and Hao, W.: First observation-based estimates of cloud-free aerosol radiative forcing across China, J. Geophys. Res., 115, D00K18, https://doi.org/10.1029/2009jd013306, 2010.

745 Liu, J., Zheng, Y., Li, Z., Flynn, C., and Cribb, M.: Seasonal variations of aerosol optical properties, vertical distribution and associated radiative effects in the Yangtze Delta region of China, J. Geophys. Res-Atmos., 117(D16), https://doi.org/10.1029/2011JD016490, 2012.

Liao, H., Chang, W., and Yang, Y.: Climatic effects of air pollutants over china: a review, Adv. Atmos. Sci. 32(1), 115-139, https://doi.org/10.1007/s00376-014-0013-x, 2015.

750 Long, C. N. and Shi, Y.: An automated quality assessment and control algorithm for surface radiation measurements, The Open Atmospheric Science Journal, 2, 23–37, https://doi.org/10.2174/1874282300802010023, 2008.

Mann, H. B.: Nonparametric tests against trend, Econometrica , 13, 245–259, 1945.

Menon, S., Hansen, J., Nazarenko, L., and Luo, Y.: Climate effects of black carbon aerosols in China and India, Science, 297, https://doi.org/10.1126/science.1075159, 2002.

755 Michalsky, J., Anderson, G., Barnard, J., Delamere, J., Gueymard, C., Kato, S., Kiedron, P., Mc Comiskey, A., and Ricchiazzi, P.: Shortwave radiative closure studies for clear skies during the atmospheric radiation measurement 2003 aerosol intensive observation period, J. Geophys. Res. Atmos., 111(D14), https://doi.org/10.1029/2005JD006341, 2006.

Nyeki, S., Wehrli, C., Gröbner, J., Kouremeti, N., Wacker, S., Labuschagne, C., Mbatha, N., and Brunke, G.: The GAW-PFR aerosol optical depth network: the 2008-2013 time series at Cape Point Station, South Africa, J. Geophys. Res. Atmos., 120(10),

760 5070-5084, https://doi.org/10.1002/2014JD022954, 2015.

Oikawa, E., Nakajima, T., Inoue, T., and Winker, D.: A study of the shortwave direct aerosol forcing using ESSP/CALIPSO observation and GCM simulation, J. Geophys. Res. Atmos., 118, 3687–3708, https://doi.org/10.1002/jgrd.50227, 2013.

Paulot, F., Paynter, D., Ginoux. P., Naik, V., and Horowitz, L. W.: Changes in the aerosol direct radiative forcing from 2001 to 2015: observational constraints and regional mechanisms, Atmos. Chem. Phys., 18, 13265–13281, https://doi.org/10.5194/acp-18-13265-2018, 2018

Qiu, Y., Liao, H., Zhang, R., and Hu, J.: Simulated impacts of direct radiative effects of scattering and absorbing aerosols on surface-layer aerosol concentrations in China during a heavily polluted event in February 2014: aerosol radiative feedbacks over the NCP, J. Geophys. Res. Atmos., 122, https://doi.org/10.1002/2016JD026309, 2017.

Randles, C. A. , Sliva, A. M. D. , Buchard, V. , Colarco, P. R. , and Flynn, C. J.: The MERRA-2 Aerosol Reanalysis, 1980 – onward, Part I: System Description and Data Assimilation Evaluation, J. Clim., 30(17), 6823, https://doi.org/10.1175/JCLI-D-16-0609.1, 2017.

Reddy, K., Kumar, D., Ahammed, Y., and Naja, M.: Aerosol vertical profiles strongly affect their radiative forcing uncertainties: study by using ground-based lidar and other measurements, Remote Sens. Lett., 4(10), 1018-1027, https://doi.org/10.1080/2150704X.2013.828182, 2013

Ricchiazzi, P., S. R. Yang, C. Gautier, and D. S.: SBDART: A research and teaching software tool for plane parallel radiative transfer in the Earth's atmosphere, Bull. Am. Meteorl. Soc., 79, 2101–2114, https://doi.org/10.1175/1520-0477(1998)0792.0.CO;2, 1998.

Rosenfeld, D.: TRMM observed first direct evidence of smoke from forest fires inhibiting rainfall, Geophys. Res. Lett., 26, 3105-3108, https://doi.org/10.1029/1999gl006066, 1999.

Sanchez, G., Serrano, A., Cancillo, M., and Garcia, J.: Pyranometer thermal offset: measurement and analysis, J. Atmos. Ocean. Technol., 32(2), 234-246, https://doi.org/10.1175/jtech-d-14-00082.1, 2015.

Shettle, E. P., and R. W. Fenn, 1975: Models of the atmospheric aerosols and their optical properties. AGARD Conf. Proc., Optical Propagation in the Atmosphere, Lyngby, Denmark, NATO Advisory Group for Aerospace Research, 2.1-2.16

Song, J. Y., Quality Evaluations and feature analysis of radiation data at background stations in China, Master thesis, Chinese Academy of Meteorological Sciences, 2013.

Song, Z., Fu, D., Zhang, X., Wu, Y., Xia, X., and He, J.: Diurnal and seasonal variability of PM2.5 and AOD in North China plain: Comparison of MERRA-2 products and ground measurements, Atmos. Environ., 191,70-78, https://doi.org/10.1016/j.atmosenv.2018.08.012, 2018.

Su, W., Corbett, J., Eitzen, Z., and Liang, L.: Next-generation angular distribution models for top-of-atmosphere radiative flux calculation from CERES instruments: methodology, Atmos. Meas. Tech., 8(2), 611-632, https://doi.org/10.5194/amtd-8-4489-2015, 2015.

Sundström, A., Arola, A., Kolmonen, P., Xue, Y., De Leeuw, G., and Kulmala, M. On the use of a satellite remote-sensing-based approach for determining aerosol direct radiative effect over land: a case study over China, Atmos. Chem. Phys., 15(1), 505-518, https://doi.org/10.5194/acp-15-505-2015, 2015.

795   Tian, P., Zhang, L., Cao, X., Sun, N., and Wang, H.: Enhanced bottom-of-the-atmosphere cooling and atmosphere heating efficiency by mixed-type aerosols: a classification based on aerosol nonsphericity, J. Atmos. Sci., 75(1), 113-124, https://doi.org/10.1175/JAS-D-17-0019.1, 2018a.

Tian, P., Zhang, L., Ma, J., Tang, K., Xu, L., Wang, Y., Cao, X., Liang, J., Ji, Y., Jiang, H., and Zhang, R.: Radiative absorption enhancement of dust mixed with anthropogenic pollution over east Asia, Atmos. Chem. Phys., 18(11), 7815-7825,
800   https://doi.org/10.5194/acp-18-7815-2018, 2018b.

Tilstra, L. G., and ~~P.~~ Stammes P. ~~: Earth.~~ : Earth reflectance and polarization intercomparison between SCIAMACHY onboard Envisat and POLDER onboard ADEOS-2, J. Geophys. Res., 112, D11304, https://doi.org/10.1029/2006JD007713,2007.

Twomey, S.: The influence of pollution on the shortwave albedo of clouds, J. Atmos. Sci., 34, 1149-1152, https://doi.org/10.1175/1520-0469(1977)034<1149:TIOPOT>2.0.CO;2. , 1977.

805   Thomas, G. E., Chalmers, N., Harris, B., Grainger, R. G., and Highwood, E. J.: Regional and monthly and clear-sky aerosol direct radiative effect (and forcing) derived from the GlobAEROSOL-AATSR satellite aerosol product, Atmos. Chem. Phys., 13(1), 393-410, https://doi.org/10.5194/acp-13-393-2013, 2013.

Wang, J., and Christopher, S.: Mesoscale modeling of central american smoke transport to the United States: 2. smoke radiative impact on regional surface energy budget and boundary layer evolution, J. Geophys. Res., 111(D14),_D14S92,
810   https://doi.org/10.1029/2005JD006720, 2006.

Wang, J., and Martin. T.: Satellite characterization of urban aerosols: importance of including hygroscopicity and mixing state in the retrieval algorithms, J. Geophys. Res., 112, D17203, https://doi.org/10.1029/2006JD008078, 2007.

Wang, J., Van, d., and Reid, J.: A conceptual model for the link between Central American biomass burning aerosols and severe weather over the South Central United States, Environ. Res. Lett., 4(1), 015003, https://doi.org/10.1088/1748-
815   9326/4/1/015003, 2009.

Wang, P., W. H. Knap, P. Kuipers Munneke, and P. Stammes.: Clear-sky shortwave radiative closure for the Cabauw Baseline Surface Radiation Network site, Netherlands, J. Geophys. Res., 114, D14206, https://doi.org/10.1029/2009JD011978, 2009.

Wang, X., Dickinson, R., Su, L., Zhou, C., and Wang, K.: PM2.5 pollution in China and how it has been exacerbated by terrain
820   and meteorological conditions, Bull. Am. Meteorl. Soc., 99(1), 105-120, https://doi.org/10.1175/BAMS-D-16-0301.1, 2018.

Wang, Y., Xin, J., Pan, Y., Ji, D., Liu, Z., Wen, T., Wang, Y., Li, X., Sun, Y., Wang, P., Wang, G., Wang, X., Cong, Z., Song, T., Hu, B., Wang, L., Tang, W., Gao, W., Guo, Y., Miao, H., Tian, S., and Wang, L.: The campaign on atmospheric aerosol research network of China: Care-China, Bull. Am. Meteorl. Soc., 141104074432007, https://doi.org/10.1175/BAMS-D-14-00039.1, 2014.

825   Wang, Y., Duan, J., Xie, X., He, Q., Cheng, T., Mu, H., Gao, W., and Li, X.: Climatic factors and their availability in estimating long-_-=-term variations of fine particle distributions over East China, J. Geophys. Res. Atmos., 124, https://doi.org/10.1029/2018JD029622, 2019.

Wu, Y., Zhang, J., Zhang, R., and Zhang, X.: Ground-based remote sensing of aerosol climatology in China: aerosol optical properties, direct radiative effect and its parameterization, Atmos. Environ., 124(2015), 243-251, https://doi.org/10.1016/j.atmosenv.2015.05.071, 2016.

Xia, X., Chen, H., Li, Z., Wang, P., and Wang, J.: Significant reduction of surface solar irradiance induced by aerosols in a suburban region in northeastern China, J. Geophys. Res. Atmos., 112(D22S02), https://doi.org/10.1029/2006JD007562, 2007.

Xia, X., Che, H., Zhu, J., Chen, H., Cong, Z., Deng, X., Fan, X., Fu, Y., Goloub, P., Jiang, H., Liu, Q., Mai, B., Wang, P., Wu, J., Bei, N., Hu, B., Liu, S., Zhou, M., Wang, Q., Li, X., Liu, L., Feng, T., Liu, Z., Wang, Y., Cao, J., Tie, X., Wang, J., Molina, L. T., and Li, G.: Aerosol–radiation feedback deteriorates the wintertime haze in the North China Plain, Atmos. Chem. Phys., 19, 8703-8719, https://doi.org/10.5194/acp-19-8703-2019, 2019.

Xia, X., Z. Li, B. Holben, P. Wang, T. Eck, H. Chen, M. Cribb, and Y. Zhao: Aerosol optical properties and radiative effects in the Yangtze Delta region of China, J. Geophys. Res., 112, D22S12, https://doi.org/10.1029/2007JD008859,2007.

Xie, Y., Zhang, Y., Xiong, X., Qu, J., and Che, H.: Validation of MODIS aerosol optical depth product over china using CARSNET measurements, Atmos. Environ., 45(33), 5970-5978, https://doi.org/10.1016/j.atmosenv.2011.08.002, 2011.

Xin, J., Wang, Y., Li, Z., Wang, P., and Hu, B.: Aerosol optical depth (AOD) and Ångström exponent of aerosols observed by the Chinese sun hazemeter network from August 2004 to September 2005, J. Geophys. Res. Atmos., 112(D5), 1703-1711, https://doi.org/10.1029/2006JD007075, 2007.

Ye, G., Wu, Y., and Liu, B.: Spatial and temporal distribution characteristics of fog and haze in Fuzhou (in Chinese), Chin. Environ. Science Technol. v.33(10), 114-119, 2010.

Yin, K., Cloud computing: Concept, model, and key technologies, ZTE Technology Journal, 16(4),18-23,2010

Yu, H., Dickinson, R., Chin, M., Kaufman, Y., Zhou, M., Tian, Y., Dubovik, O., and Holben, B.: direct radiative effect of aerosols as determined from a combination of MODIS retrievals and GOCART simulations, J. Geophys. Res.,109, D03206, https://doi.org/10.1029/2003JD003914

Yu, H., Kaufman, Y. J., Chin, M., Feingold, G., Remer, L. A., Anderson, T. L., Balkanski, Y., Bellouin, N., Boucher, O., Christopher, S., Decola, P., Kahn, R., Koch, D., Loeb, N., Reddy, M. S., Schulz, M., Takemura, T., and Zhou, M.: A review of measurement-based assessments of the aerosol direct radiative effect and forcing, Atmos. Chem. Phys., 6(3), 613-666, https://doi.org/10.5194/acp-6-613-2006, 2006.

Yu, X., Ma, J., Kumar, R., K. Zhu, B., An, J., He, J., and Li, M.: Measurement and analysis of surface aerosol optical properties over urban Nanjing in the Chinese Yangtze River Delta, Sci. Total Environ., 542, 277-291, https://doi.org/10.1016/j.scitotenv.2015.10.079, 2016a.

Yu, X., Kumar, K., Lyu R., and Ma, J.: Changes in column aerosol optical properties during extreme haze-fog episodes in January 2013 over urban Beijing, Environ. Pollut., 210, 217-226, https://doi.org/10.1016/j.envpol.2015.12.021, 2016b.

Yu, Y., Xia, X., and Chen, H.: A comparison between measured and modeled clear-sky surface solar irradiance (in Chinese), Aeta Energiae Solaris Sinica, 28(3): 233-240, 2007.

Yu, Y., and Song, M.: Big data (3), ZTE Technology Journal. 19(3), 57-62, https://doi.org/10.3969/j.issn.1009-6868.2013.03.013, 2013

Song, Z., Fu, D., Zhang, X., Wu, Y., Xia., X., He, J., Han, X., Zhang, R., and Che, H.: Diurnal and seasonal variability of PM2.5, and AOD in North China plain: Comparison of MERRA-2 products and ground measurements, Atmos. Environ.,

865 191,70-78, https://doi.org/10.1016/j.atmosenv.2018.08.012, 2018.

Song, J.: Quality evaluations and feature analysis of radiation data at background stations in China, Chinese Academy of Meteorological Sciences, Master Thesis, 2013.Zhang, J. L., Reid, S. J., Contreras, R. A., and Xian, P.: Has China been exporting less particulate air pollution over the past decade? Geophys. Res.Lett., 44, https://doi.org/ 10.1002/2017GL072617, 2017.

870 Zhou, C., Zhang, H., Zhao, S., and Li, J.: On effective radiative forcing of partial internally and externally mixed aerosols and their effects on global climate, J. Geophys. Res. Atmos., 123, https://doi.org/10.1002/2017JD027603, 2018.

Zhang, M., Ma, Y., Gong, W., Liu, B., Shi, Y., and Chen, Z.: Aerosol optical properties and radiative effects: assessment of urban aerosols in central China using 10-year observations, Atmos. Environ.,182, 275-285, https://doi.org/10.1016/j.atmosenv.2018.03.040, 2018.

875 Zhuang, B., Wang, T., Liu, J., Che, H., Han, Y., Fu, Y., Li, S., Xie, M., Li, M., Chen, P., Chen, H., Yang, X., and Sun, J.: The optical properties, physical properties and direct radiative forcing of urban columnar aerosols in the Yangtze River Delta, China, Atmos. Chem. Phys., 18(2), 1419-1436, https://doi.org/10.5194/acp-18-1419-2018, 2018.

Table 1: Summary of the acronyms.

ADRF	Aerosol direct radiative forcing (W m^{-2})
SSA	Single scattering albedo (unit less)
ASY	Asymmetry parameter (unit less)
AOD	Aerosol optical depth (unit less)
F_u_toa	Upward radiative fluxes at the top of atmosphere (W m^{-2})
F_d_sur	Downward radiative fluxes at the surface (W m^{-2})
F_u_sur	Upward radiative fluxes at the surface (W m^{-2})

880

Table 2: Satellite and reanalysis datasets used in the study.

Parameters	Products	Sensors/Models	Spatial Resolution	Temporal Resolution
AOD	MOD04 L2	Terra MODIS	0.1°×0.1°	instantaneous
SSA	tavg1_2d_aer_Nx	MERRA-2	0.625°×0.5°	hourly
Surface albedo	MCD43C3	Terra+Aqua MODIS	0.052°×0.052°	daily
Upward TOA radiative flux	SSF	Terra CERES	20km	instantaneous
Meteorological data	ERA-Interim	ECMWF	0.125°×0.125°	hourly

Table 3: The geographical characteristics of observation sites for sunphotometer and pyranometer.

Location	Lon/Lat	Instrument (Product)	Observing Period
Pudong (Urban)	121.79°E/31.05°N	Sunphotometer (SSA)	2010.12-2012.10 2014.1-2015.11
Taihu (Rural)	120.22°E/31.42°N	Sunphotometer (SSA)	2005.1-2012.12 2015.1-2016.12
Xuzhou (Urban)	117.14°E/34.22°N	Sunphotometer (SSA)	2013.8-2016.12
Baoshan (Urban)	121.45°E/31.4°N	Pyranometer (F_d_sur)	2014.1-2016.12
Fuzhou (Urban)	119.29°E/26.08°N	Pyranometer (F_d_sur)	2014.1-2016.12
Yong'an (Rural)	117.37°E/25.98°N	Pyranometer (F_d_sur)	2014.1-2016.12

885 **Table 3: The geographical characteristics, observing period, sample number of sunphotometer sites. The fitted regression equations between MERRA-2 and sunphotometer SSA are also shown here. In the equation, x represents SSA sample, y represents fitted value of SSA.**

Location	Lon/Lat	Observing period	Sample number	Fitted regression equation between MERRA-2 and sunphotometer SSA
Xuzhou (Urban)	117.14°E/34.22°N	2013.8-2016.12	514	y=0.02+0.94x
Shouxian (Rural)	116.78°E/32.56°N	2008.5-2008.12	26	y=-0.45+1.46x
Hefei (Urban)	117.16°E/31.91°N	2005.11-2005.12 2008.1-2008.11	19	y=0.09+0.85x
Taihu (Rural)	120.22°E/31.42°N	2005.1-2012.12 2015.1-2016.12	230	y=0.2+0.75x
Pudong (Urban)	121.79°E/31.05°N	2010.12-2012.10 2014.1-2015.11	84	y=0.49+0.46x
Hangzhou (Urban)	120.16°E/30.29°N	2008.4-2009.2	45	y=0.38+0.57x

890

Table 4: Errors induced by different input parameters in ASY, radiative flux (F_d_sur, F_u_sur) and ADRF. Here, the uncertainties of input parameters (AOD, Albedo, CERES F_u_toa) are from literatures and the uncertainty of SSA is from validation in Section 4.

Parameter	Uncertainty	Errors in ASY	Errors in F_d_sur	Errors in F_u_sur	Errors in ADRF
AOD	±20%[a]	-3.7%~1.7%	~4.5%	~4.4%	~15.4%
SSA	±10%	-19%~23%	~12%	~12%	~24%
Albedo	±5%[b]	-3.7%~1.7%	~0.7%	~5.9%	~3%
CERES F_u_toa	±1.6%[c]	-1.8%~1.7%	~0.4%	~0.4%	~1.5%

895 [a] He et al. (2010).

[b] Cescatti et al. (2012).

[c] Su et al. (2015).

Figure 1: The map of research area, <u>topography,</u> major lakes and <u>mountains</u> ~~topography~~ in East China ~~are shown~~. The ~~blue triangles denote the locations of sunphotometers and the~~ red circles ~~are~~ <u>denotes the locations of three</u> pyranometers <u>(Baoshan, Fuzhou and Yong'an)</u>. This figure was generated by ArcGIS, version 10.2. Map source: Map World (National Platform for Common Geospatial Information Services, <u>www.tianditu.gov.cn</u>~~/~~) .
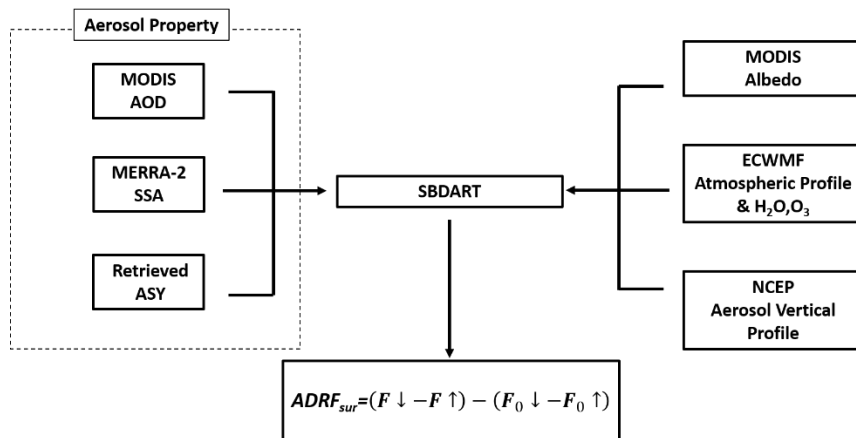
Figure 2: A schematic diagram to simulate ADRF based on satellite and reanalysis datasets.

The diagram shows:

- **Aerosol Property** (dashed box containing):
  - MODIS AOD
  - MERRA-2 SSA
  - Retrieved ASY

- These feed into **SBDART**

- Also feeding into SBDART:
  - MODIS Albedo
  - ECWMF Atmospheric Profile & H_2O, O_3
  - NCEP Aerosol Vertical Profile

- SBDART outputs:

$$ADRF_{sur} = (F \downarrow - F \uparrow) - (F_0 \downarrow - F_0 \uparrow)$$

Pudong

N=85
R=0.56
y=0.46x+0.49

Taihu

N=230
R=0.68
y=0.75x+0.20

Xuzhou

N=514
R=0.76
y=0.94x+0.02

MERRA-2 SSA
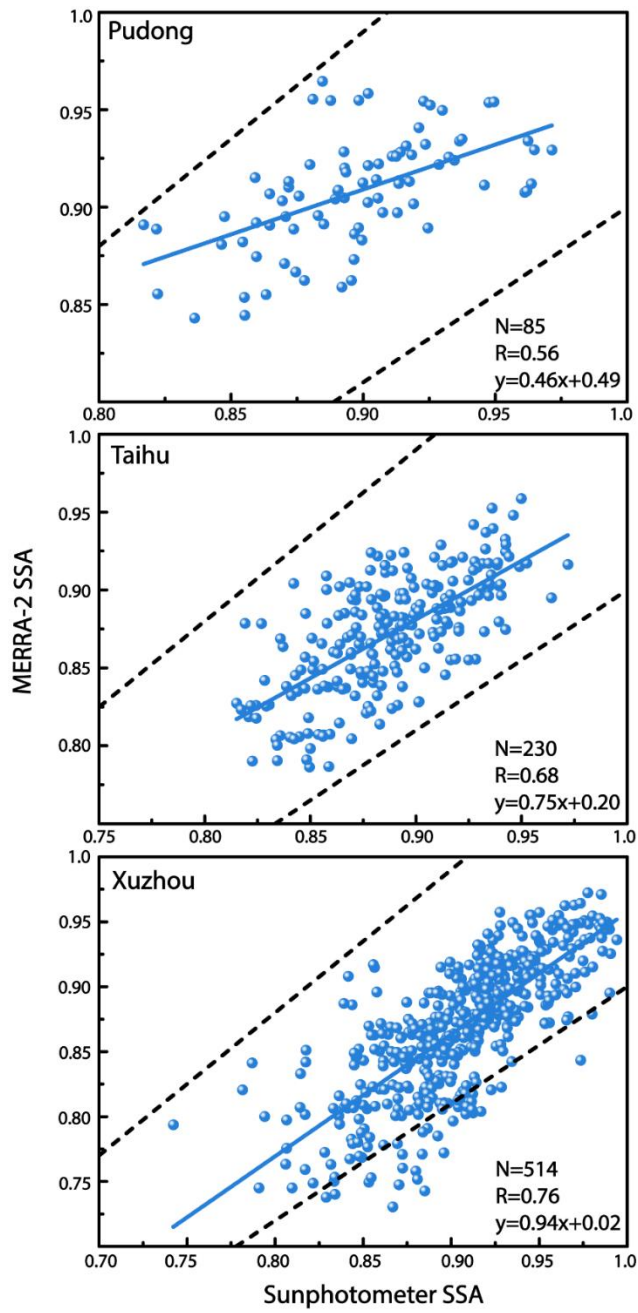
Sunphotometer SSA

Figure 3: The scatter plots of SSA between MERRA-2 and sunphotometer in Pudong, Taihu, and Xuzhou. The blue line is the fitting curve while dashed lines are the range of ±10% relative error.
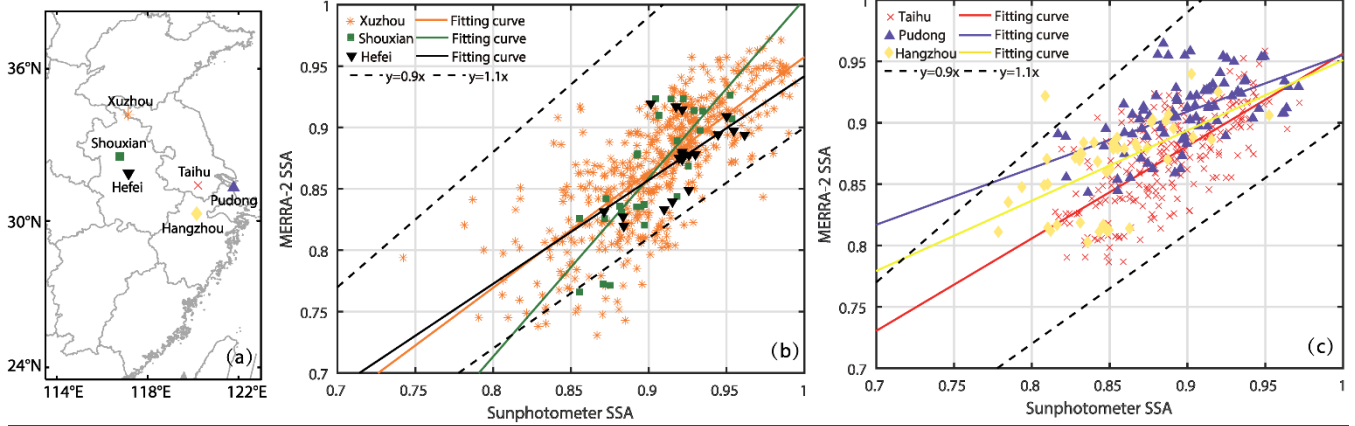
Figure 3: (a) The location of six sunphotometer sites over East China. (b) The scatter plots of SSA between MERRA-2 and sunphotometer in Xuzhou, Shouxian and Hefei. Orange dots represent Xuzhou samples and orange line is the fitting curve of Xuzhou samples while green represents Shouxian and black represents Hefei. Dashed lines are the range of ±10% relative error. (c) The scatter plots of SSA between MERRA-2 and sunphotometer in Taihu, Pudong and Hangzhou. Red dots represent Taihu samples and red line is the fitting curve of Taihu samples while purple represents Pudong and yellow represents Hangzhou. Dashed lines are the range of ±10% relative error.

ASYa(0.1) → F_u_toa_a; ASYb(0.9) → F_u_toa_b

$(F\_u\_toa\_a - F\_u\_toa) \times (F\_u\_toa\_b - F\_u\_toa) < 0$ —N→ ASY = NaN

Y

$ASYc = \frac{1}{2}(ASYa + ASYb)$
ASYc → F_u_toa_c

$|F\_u\_toa\_c - F\_u\_toa| < 1$ ····Y····

N

ASYa = ASYc
F_u_toa_a = F_u_toa_c ←N— $(F\_u\_toa\_a - F\_u\_toa) \times (F\_u\_toa\_c - F\_u\_toa) < 0$ —Y→ ASYb = ASYc
F_u_toa_b = F_u_toa_c

ASY = ASYc
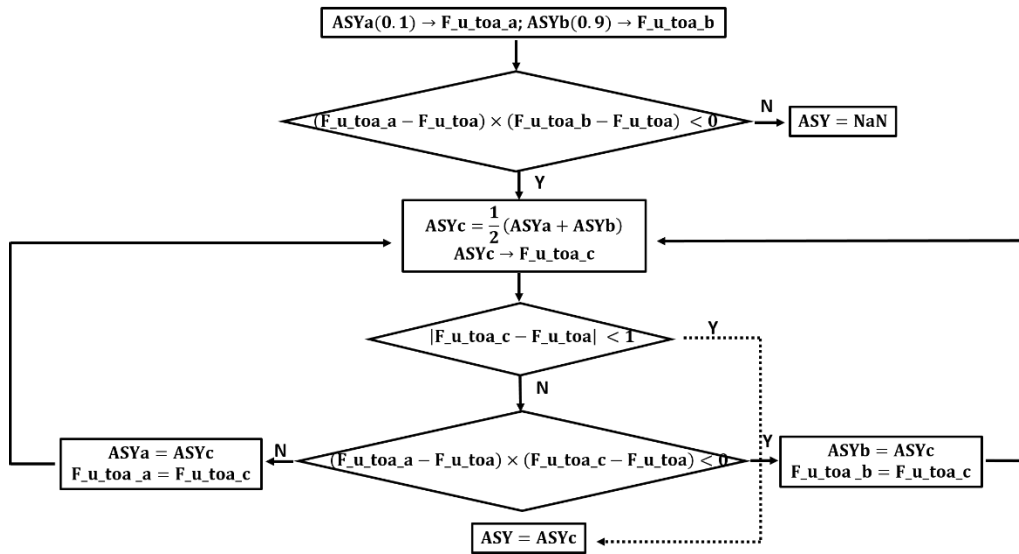
Figure 4: A detailed workflow of binary search used in ASY retrieval.

43
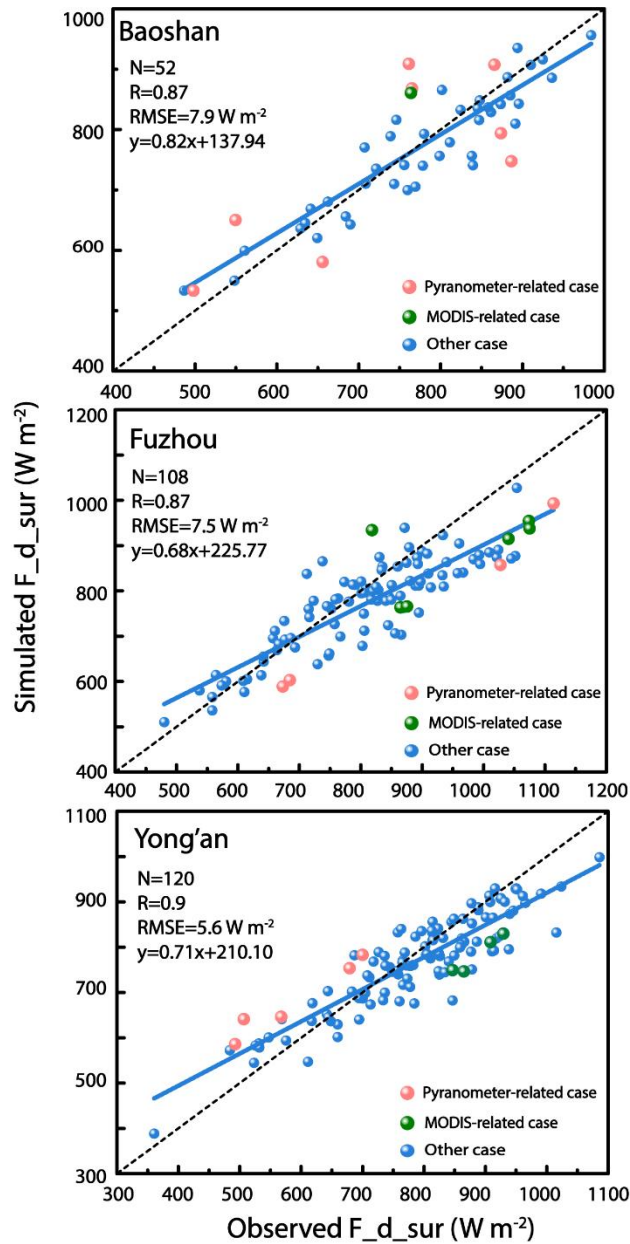
Figure 5: The scatter plots between observed F_d_sur by pyranometers and simulated F_d_sur by SBDART in Baoshan, Fuzhou, and Yong'an. The blue line the is fitting curve and the dashed line represents y=x. The red dots denote the specific case in which the pyranometer captures the fluctuation of F_d_sur by clouds during one hour. The olive green dots denote the specific case in which the site is completely covered by clouds, deduced from MODIS true color map composed by 1, 4 and 3 channels. The blue dots represent the other ordinary case.

(a)

Unit: W m^{-2}

(b)
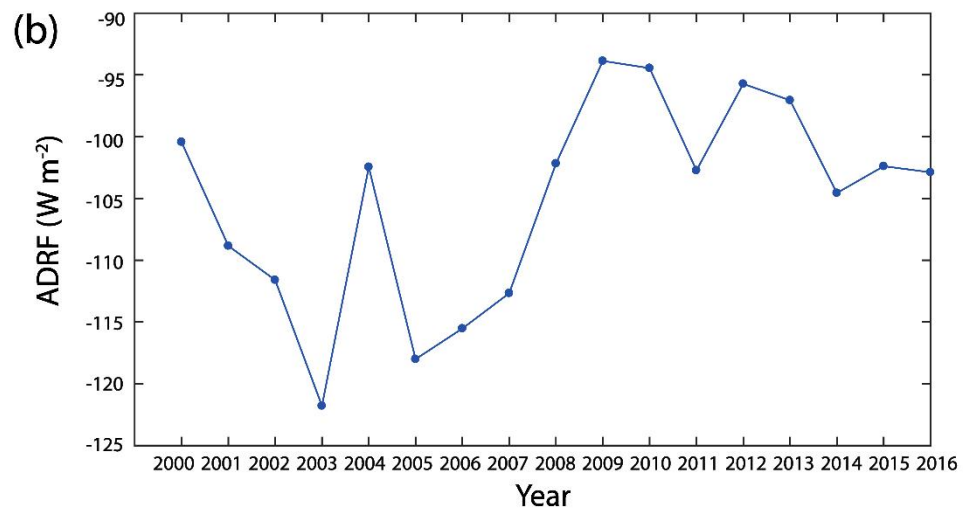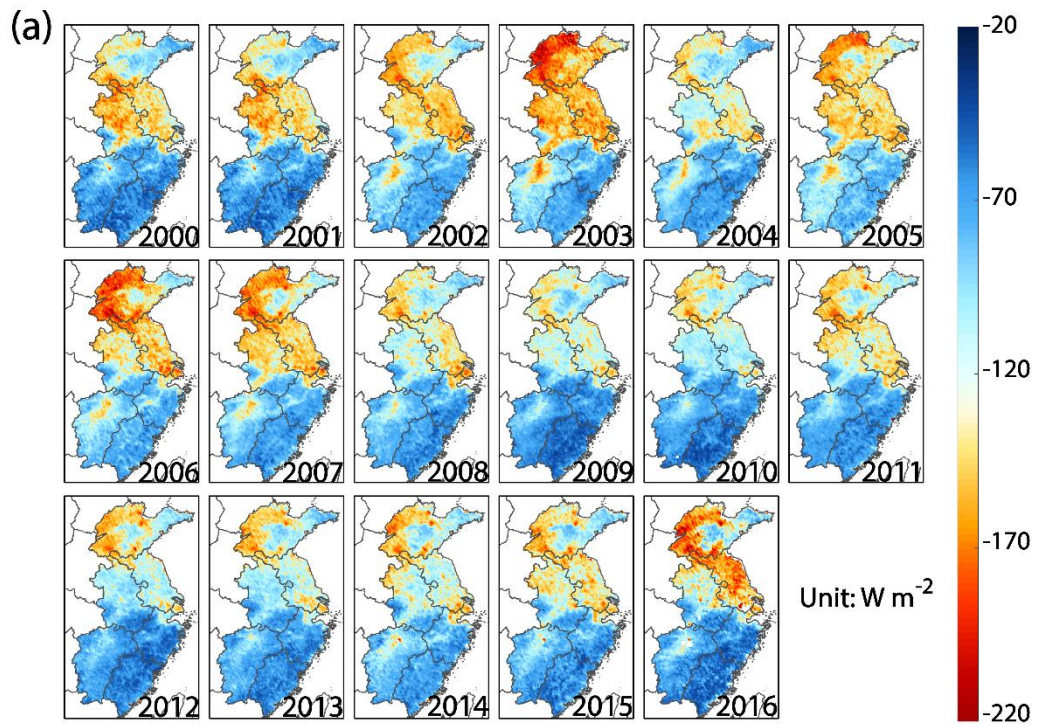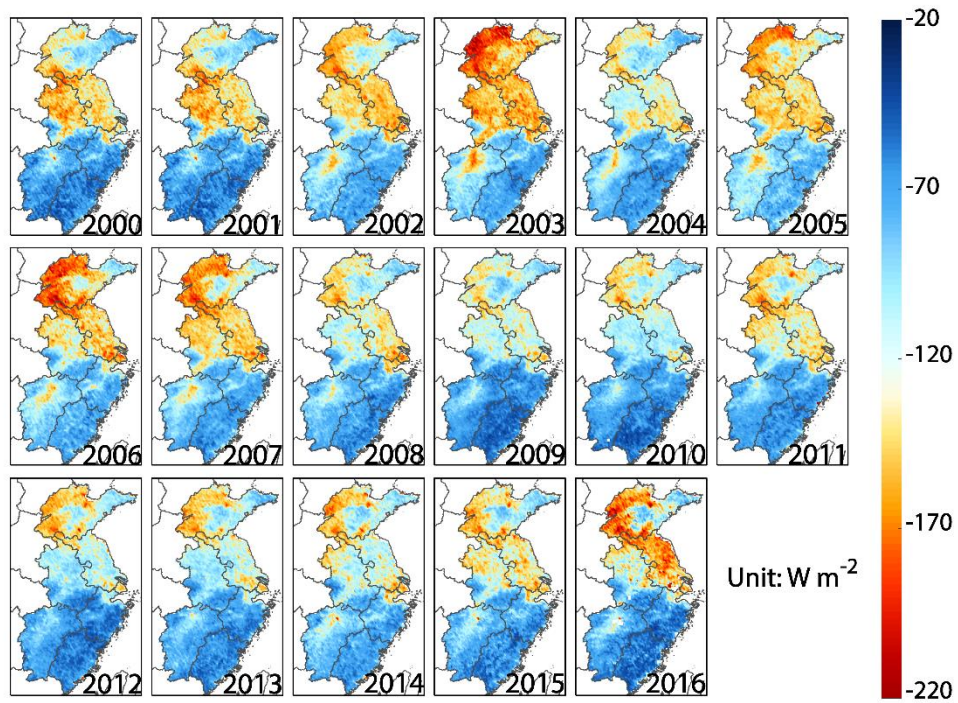
Figure 6: (a)Annual Yearly mean ADRF distributions during 2000-2016 over East China (unit: W m^{-2}). (b)The changes of annual regional mean ADRF during 2000-2016 over East China.
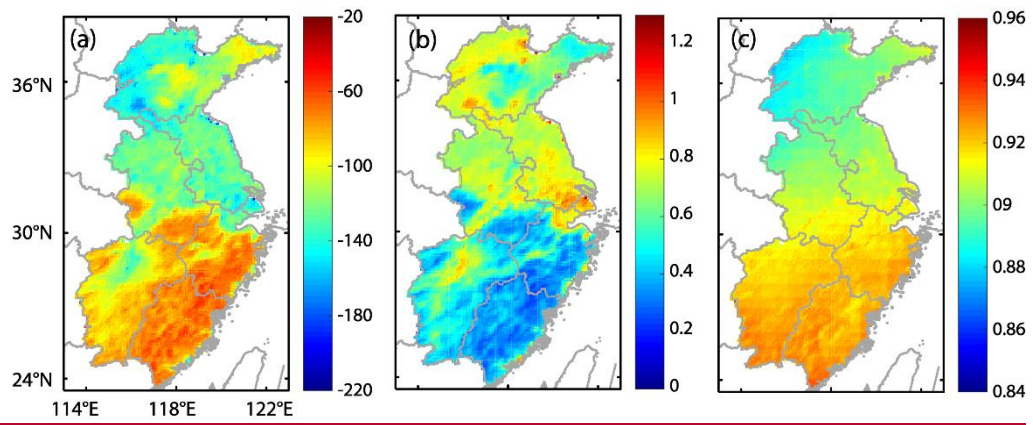
Figure 7: Averaged spatial distribution of (a)ADRF (unit: W m⁻²), (b)AOD and (c)SSA during 2000-2016 in the East China.

940
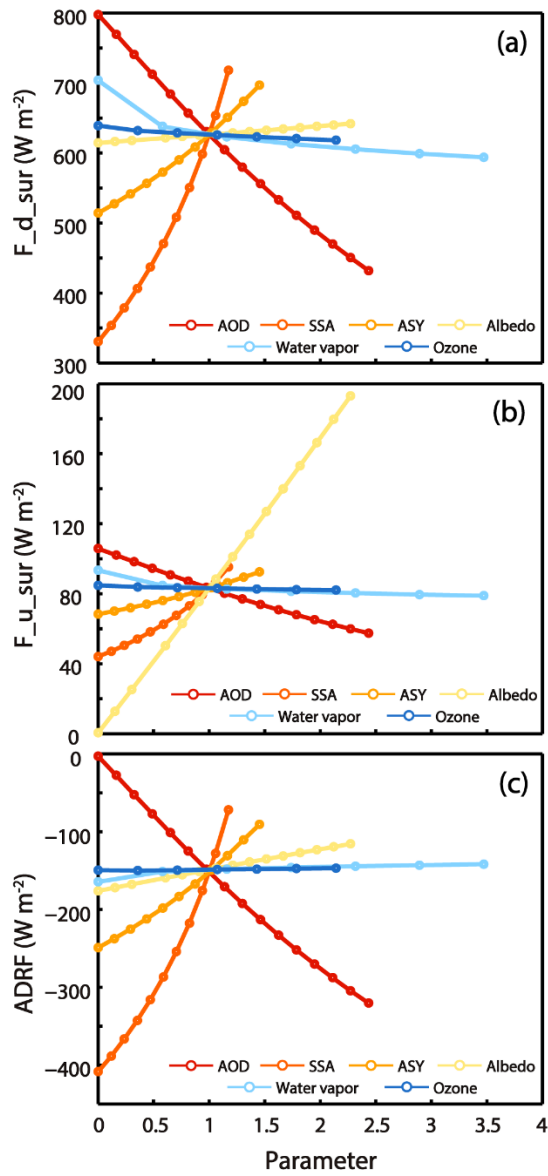
Figure 7: The response of F_d_sur, F_u_sur, ADRF to different parameters (AOD, SSA, ASY, albedo, columnar water vapor and ozone) in the sensitivity test. The X-axis value shows the ratio of the input to the actual value to dimensionalize the parameters for comparison.

945

48
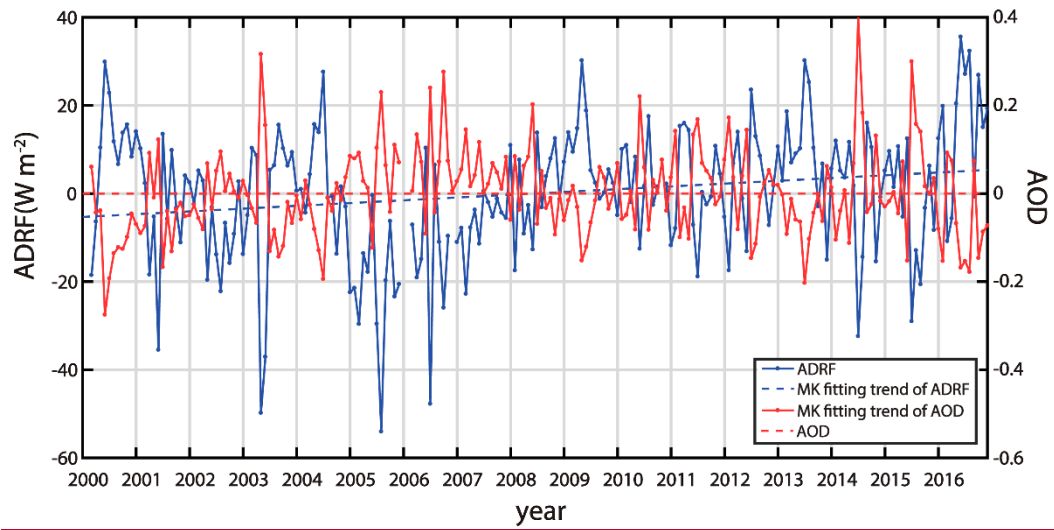
Figure 8: The time series of monthly mean ADRF (blue) and AOD (red) in East China from 2000 to 2016. Dashed lines represent the Mann-Kendell (MK) fitting trend of ADRF and AOD.

950
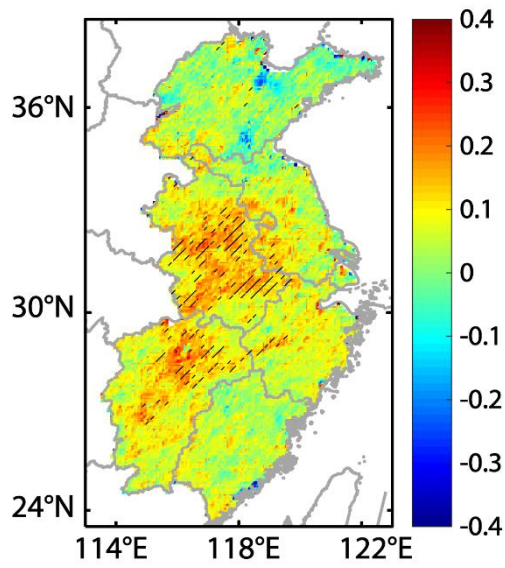
Figure 9: The spatial distribution of ADRF trend in East China during 2000-2016 (unit: W m^{-2} month^{-1}). Hatched regions represent those exceeding the 90% significance level.

Supplementary ~~of~~Information

Retrieval of Gridded Aerosol Direct Radiative Forcing Based on Multi-platform Datasets

Yanyu Wang[1], Rui Lyu[1], Xin Xie[1], Ze Meng[2], Meijin Huang[2,3], Junshi Wu[3,4], Haizhen Mu[3,4], Qiu-Run Yu[4,5], Qianshan He[4,3,5,6]*, Tiantao Cheng[7,6,8,1,7] *

[1]Shanghai Key Laboratory of Atmospheric Particle Pollution and Prevention (LAP³), Department of Environmental Science and Engineering, Institute of Atmospheric Sciences, Fudan University, Shanghai, 200438, China

[2]School of Oceanography, Shanghai Jiao Tong University, Shanghai, 200030, China

[2,3]Fujian Meteorological Observatory, Fuzhou, 350001, China

[3,4]Shanghai Meteorological Service, Shanghai, 200030, China

[4,5]Key Laboratory of Meteorological Disaster, Ministry of Education (KLME)/Joint International Research Laboratory of Climate and Environment Change (ILCEC), Nanjing University of Information Science and Technology, Nanjing, 210044, China

[5,6]Shanghai Key Laboratory of Meteorology and Health, Shanghai, 200030, China.

[6,7]Department of Atmospheric and Oceanic Sciences, Institute of Atmospheric Sciences, Fudan University, Shanghai, 200438, China

[7,8]Shanghai Institute of Eco-Chongming (SIEC), Shanghai, 200062, China

Correspondence to: Qianshan He (oxeye75@163.com); Tiantao Cheng(ttcheng@fudan.edu.cn).

This Supplementary Information (SI) includes 4̶3̶ figures.

975 **Supplementary Figures:**

Figure S1. ~~The boxplot of MERRA-2 SSA and sunphotometer in Pudong, Taihu, and Xuzhou.~~ Sketch map of aerosol vertical profile.
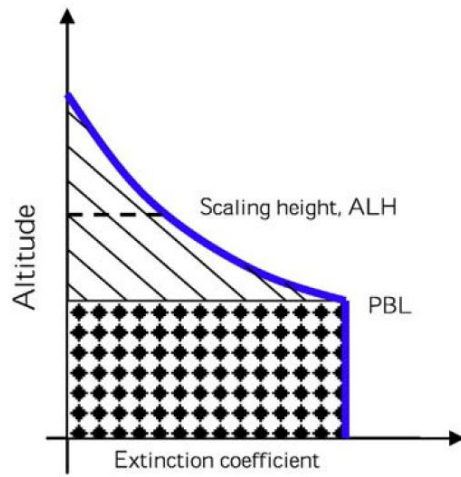
Figure S2. ~~48 h backward trajectories of air mass by HYSPLIT 4, which are terminating at Fuzhou at 500m altitude level.~~ MODIS Terra true color map composed by 1, 4, and 3 channels on October 18, 2014 (https://worldview.earthdata.nasa.gov/).

980 **Figure S3.** ~~48 h backward trajectories of air mass arriving at Yong'an at 500m altitude level and calculated every 24 h from October 22 to October 24, 2015.~~ The response of downward radiative fluxes at the surface (F_d_sur), upward radiative fluxes at the surface (F_u_sur), aerosol direct radiative forcing (ADRF) to different parameters (AOD, SSA, ASY, albedo, columnar water vapor and ozone) in the sensitivity test.

Figure S4. The occurrence frequency of annual ADRF for each grid cell in the North and South of East China during 2000-
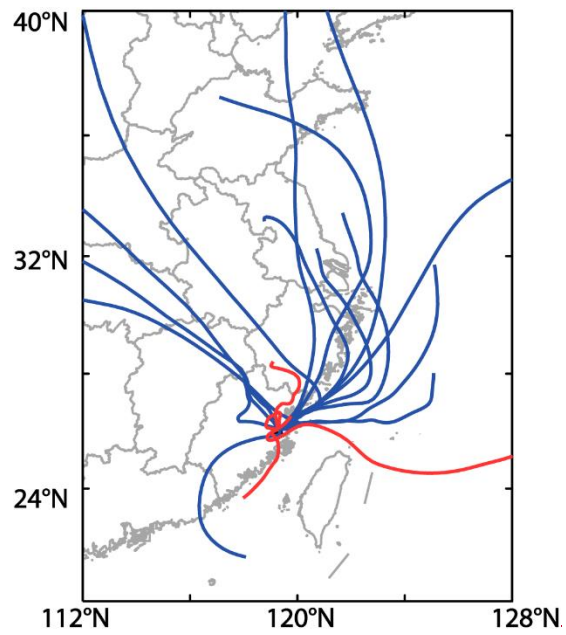985 2016.

52
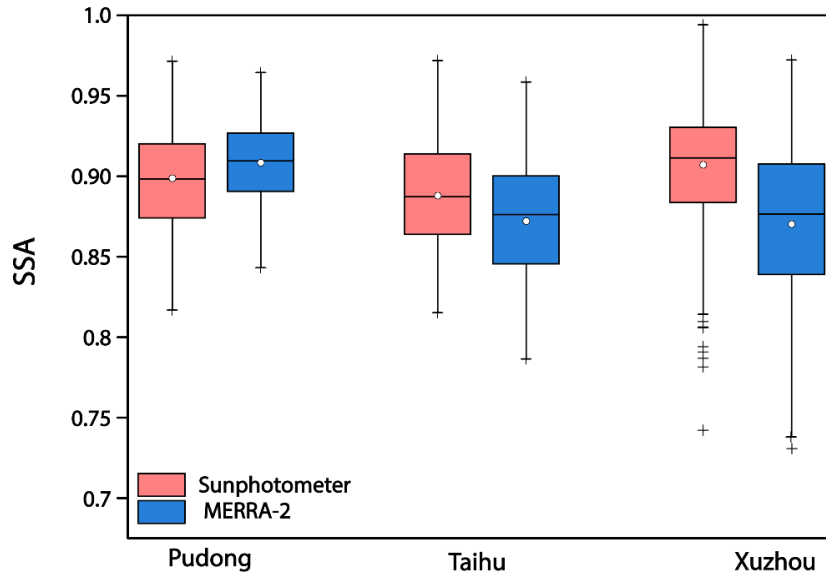
Figure S1. The boxplot of MERRA-2 SSA and sunphotometer in Pudong, Taihu, and Xuzhou. The central marks in each box are the median value while the lower and upper edges of the boxes indicate 25th and 75th percentiles. The whiskers show extreme values and the outliers are maked with "+".
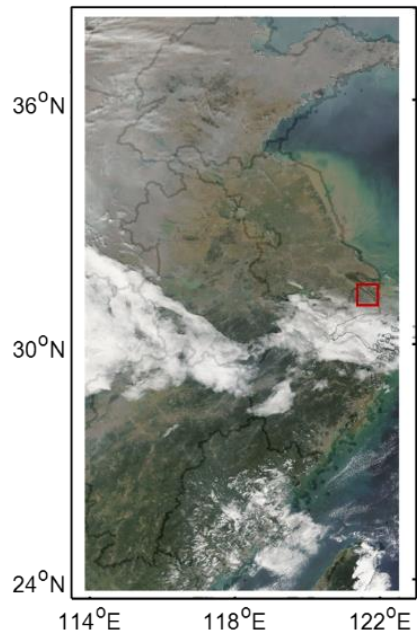
Figure S1. Sketch map of aerosol vertical profile (He et al., 2008). Two-layer aerosol model is characterized by aerosol well-mixed in the PBL and exponential decay of the aerosol extinction coefficient with altitude above the top of PBL.

1000

1005

Figure S2. MODIS Terra true color map composed by 1, 4, and 3 channels on October 18, 2014 (https://worldview.earthdata.nasa.gov/). The red rectangle box (40*40km) is the MODIS AOD average window in Baoshan pyranometers site.

NOAA HYSPLIT MODEL
Backward trajectories ending at 0200 UTC 24 Oct 15
GDAS Meteorological Data
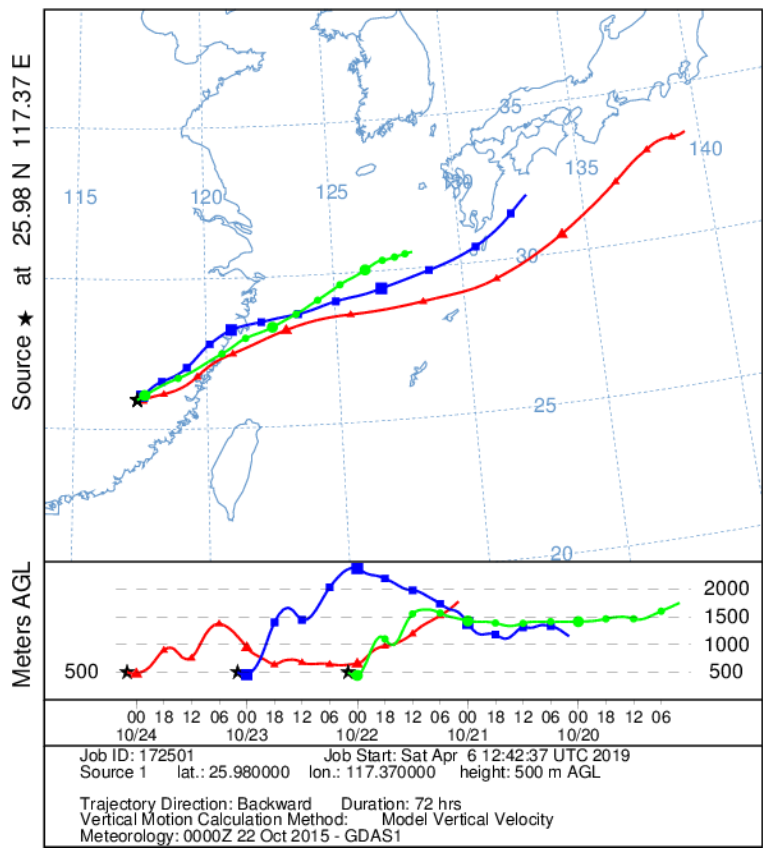
Job ID: 172501   Job Start: Sat Apr 6 12:42:37 UTC 2019
Source 1   lat.: 25.980000   lon.: 117.370000   height: 500 m AGL

Trajectory Direction: Backward   Duration: 72 hrs
Vertical Motion Calculation Method: Model Vertical Velocity
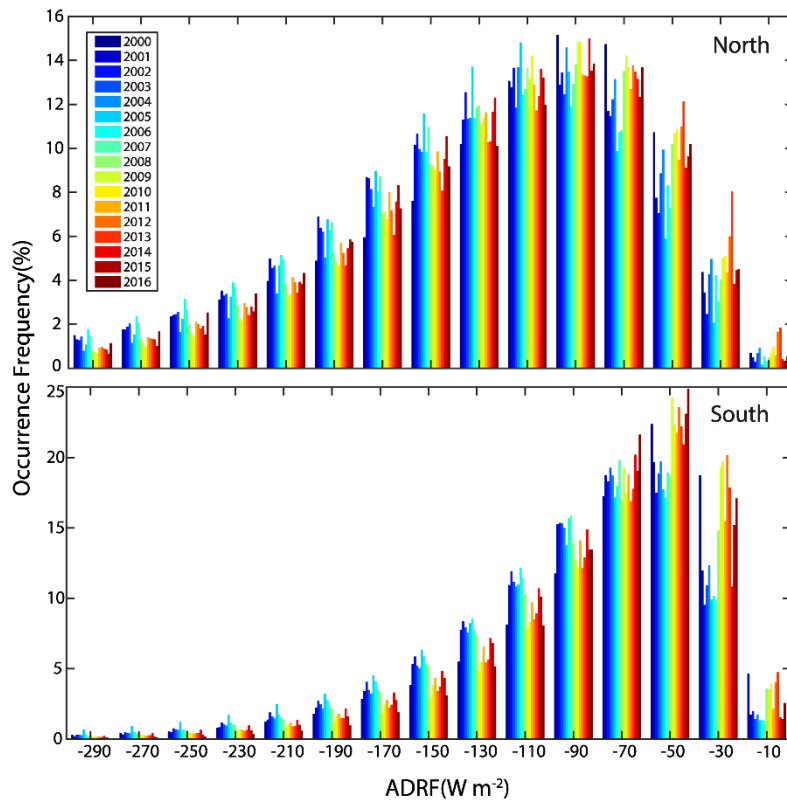Meteorology: 0000Z 22 Oct 2015 - GDAS1

1010

Figure S3. 48 h backward trajectories of air mass arriving at Yong'an at 500m altitude level and calculated every 24 h from October 22 to October 24, 2015. The start time is 2:00 (UTC) during satellite passing by.
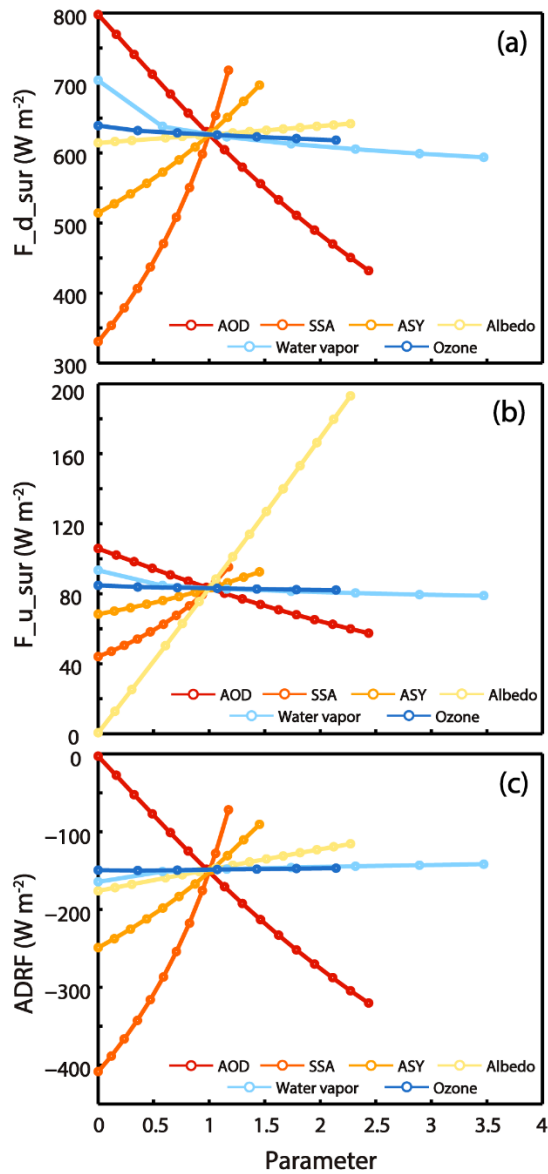
Figure S3. The response of downward radiative fluxes at the surface (F_d_sur), upward radiative fluxes at the surface (F_u_sur), aerosol direct radiative forcing (ADRF) to different parameters (AOD, SSA, ASY, albedo, columnar water vapor and ozone) in the sensitivity test. The X-axis value shows the ratio of the input to the actual value to dimensionalize the parameters for comparison.

Figure S4. The occurrence frequency of annual ADRF for each grid cell in the North and South of East China during 2000-2016.